



Precursor dynamical factors in the local lower atmosphere of Warm-Sector Heavy Rainfall over South China: Evidences from Wind Profiler Observations

- 5 Wanju Li^{1,2}, Lifang Sheng¹, Xueyan Bi², Zehao Huang³, Yali Luo³, Shiqi Xiao⁴, Chao Liu³, Yang Yang³, Jiandong Wang³, Yuanjian Yang^{3*}, Simone Lolli⁵
 - ¹College of Oceanic and Atmospheric Sciences, Ocean University of China, Qingdao, China
 - ² Guangzhou Institute of Tropical and Marine Meteorology, China Meteorological Administration, Guangzhou, China
 - ³ State Key Laboratory of Climate System Prediction and Risk Management, School of Atmospheric Physics, Nanjing University of Information Science and Technology, Nanjing 210044, China
 - ⁴ School of Atmospheric Sciences and Key Laboratory of Tropical Atmosphere-Ocean System, Ministry of Education, Sun Yat-Sen University, Zhuhai, China
 - ⁵ CNR-IMAA, Contrada S. Loja, 85050 Tito Scalo (PZ), Italy

Correspondence to: Yuanjian Yang (yyi1985@nuist.edu.cn)

Abstract. The Warm Sector Heavy Rainfall (WSHR) is one of the most typical weather events during the early summer monsoon season in South China with instantaneous torrential rain with high locality and complex atmospheric conditions, which results in difficulties in nowcasting and hazard warning. Four dynamical and thermodynamical indices within the 20 lower atmosphere are employed as precursor signals of WSHR over South China in 2019, including the Low-Level Jet Index (LLJI), the Vertical Wind Shear (VWS), the Atmospheric Lifting Intensity (ALI), and the Boundary Layer Height (BLH), by utilizing wind profiler radar and high-density surface observations. Regional heterogeneity in precursor signals are detected 1-4 hours preceding WSHR onset. Significant ALI and WVS signals in western regions are concentrated at approximately 1.5 km height, which is affected by warm, moist advection and orographic lifting. The central region, dominated by urban agglomerations, exhibited complex precursor signal interactions, where anomalies of LLJI and BLH are significant due to combined effects of urban heat island and the presence of the double LLJ at 1 km and 2.5 km, respectively. In contrast, precursor signals are moderated by the upper-level jet and moisture transport. In addition, monsoon activities and geographical factors play an important role in the spatiotemporal distribution of precursor signals. Urbanization effects on wind field at the boundary layer have significantly changed the features of dynamical precursor signals. The urban heat effect makes the low-level wind field more unstable. This research provides fundamental insights to enhance nowcasting and hazard warning for WSHR in South China.





1 Introduction

35

40

45

55

The subtropical monsoon climate prevails in South China, where torrential rainfall is one of the most dominant weather events, especially during early summer monsoon season. Warm-Sector Heavy Rainfall (WSHR) is the most common type of torrential rainfall during the summer monsoon in South China (Ding, 1994), which usually denotes heavy rainfall occurring 200–300 km away from the front system at surface on its warmer side. This type of storm occurs in the convergence region of southwest and southeast in the lower troposphere or the southwest without significant horizontal wind shear, which is free from the effects of tropical weather system such as Tropical Cyclones (TC) (Huang, 1986). There is weak baroclinic forcing and atmospheric thermodynamical instability at synoptic scale. Instantaneous and local torrential rainfall occurs under complex convective mechanisms under external forcings of rugged topography, thermodynamical and frictional contrast between land and sea, bringing challenges to forecast and reduction of natural hazard effects (Sun et al., 2019). There is limited performance of numerical weather prediction models from WSHR. Forecasts of precipitation timing, regions, and intensity still need to be improved (Chen et al., 2019; Luo et al., 2017). A recent study shows that there is limited predictability in WSHR events even with small initial errors, where the low-level wind field can result in significant deviations among 3-hour forecast results (Wu et al., 2020). Therefore, observations of key meteorological indices in higher spatiotemporal resolutions are conductive to higher nowcast accuracy in WSHR events.

Previous studies showed that WSHR in South China is highly associated with Low Level Jet (LLJ), where the convergence of low-level southerly is one of the most essential mechanisms for the occurrence of the WSHR near coastlines (Du et al., 2020; Du and Chen, 2018; Higgins et al., 1997; Stensrud, 1996; Trier et al., 2006; Zeng et al., 2019; Zhang and Meng, 2019). The LLJ are typically classified into Surface LLJ (SLLJ) and Boundary Layer Jet (BLJ), which are relevant to the synoptic weather systems in the lower troposphere. Recent studies showed that the BLJ deaccelerates and converges, with the movement from the northern South China Sea to coastal South China due to the constrast of land-sea friction and coastal topography, coupled with the SLLJ in the lower-middle troposphere (Du et al., 2020b; Du and Chen, 2018). This coupling results in strong mesoscale updraft, bringing warm and moist air from the ground to upper levels, which promotes the formation of strong convective precipitation. Zhang et al., (2022) developed a methodology to identify WSHR precursor signals at coastal regions in Guangdong Province by combining the LLJ, warm moist tongue and low-level convergence based on observational data and reanalysis data, which has been validated feasible. However, the false alarm in the hindcast experiments is due to the misidentification of vertical wind profiles. Therefore, the comprehensive study in vertical structures of the LLJ is conductive to extracting precursor signals, which improves the forecast performance in the WSHR. We used wind profiler radar data to analyze vertical profiles in high resolution right before the onset of WSHR events.

Wind profiler radar is a remote sensing instrument that operates at high altitudes without the need for balloons, It can provide instantaneous vertical wind speed profiles, particularly continuous wind profiles at middle-lower levels, especially





into the boundary layer, with a temporal resolution of several minutes. (Lolli et al, 2013, Kotthaus et al., 2023). The wind profiler radar provides the horizontal wind speed, wind direction and vertical speed and atmospheric refractivity with a high vertical resolution with short delay, which permits to continuously monitor middle-lower wind field changes associated with mesoscale weather systems (Liu et al., 2020). Studies based on torrential rainfall events in Beijing, Shanghai, Guangzhou etc.(Du et al., 2012; Li et al., 2024b; Xian et al., 2024; Zhou et al., 2022) show that the use of wind profiler radar can catch the evolution of a precipitation more efficiently, as the wind measurements can unveil changes of LLJ intensity, middle-lower level Vertical Wind Shear (VWS) and the wind fields, which grasps the occurrence of torrential rainfall.

Past research has primarily focused on a limited number of case studies or regional analyses, examining changes in LLJ, VWS, and other features. However, it has failed to present the spatiotemporal differences effectively. In this study, we select three wind profiler respectively deployed in western, central and eastern Guangdong Province to analyze evolutions of the BLH, VWS and wind speed in the cases of the WSHR events in 2019. Chapter 2 is descriptions of WSHR events in Guangdong Province, data source and calculation diagnostics. Chapter 3 offers overview of each WSHR event. Chapter 4 shows analysis in spatiotemporal characteristics of precursor signals of WSHR events. Chapter 5 discusses possible mechanisms of transregional signal difference and applications of precursor signals in the WSHR forecast. Chapter 6 provides conclusions and discussion.

2 Data and Methods

2.1 Data

80

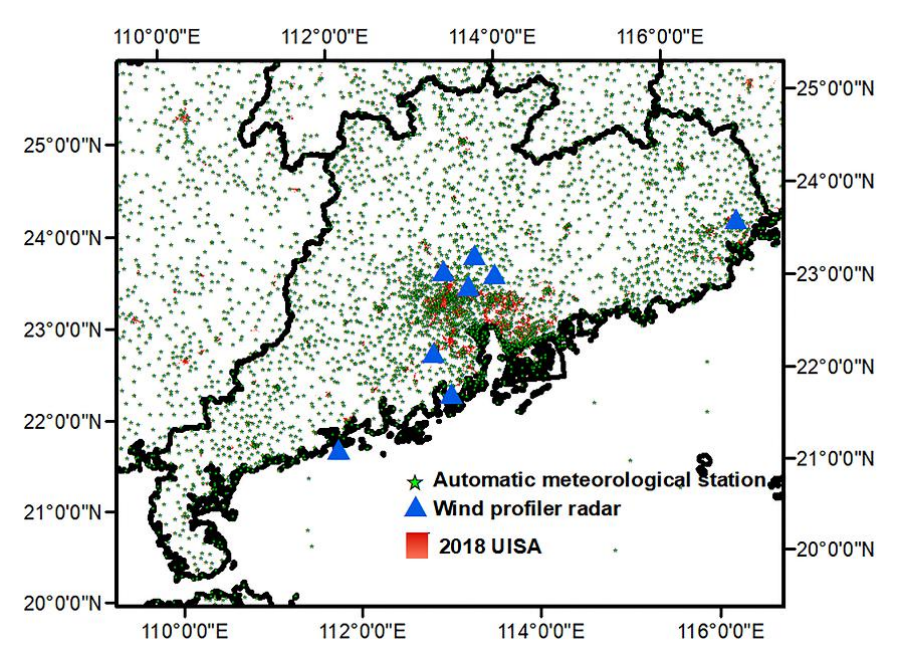
95

The wind profile radar detects wind field variables primarily by the f electromagnetic wave scattering caused by the atmospheric turbulence. These variables include wind direction, horizontal wind speed, the atmospheric refractive index structure constant (C_n^2), vertical velocity, and more. This type of radar is divided into boundary layer wind profile radar (BWPR) and tropospheric wind profile radar (TWPR) depending on detection height. Th BWPR uses LC band within 0–6 km range, with a vertical resolution of 60 m, and a temporal resolution of 5 minutes. In contrast, TWPR utilizes the PA band for 0–16 km range, with a vertical resolution of 120 m, and a temporal resolution of 6 minutes. In this study, we used real-time sounding data (ROBS) and 1-hour c-averaged data (OOBS) from eight wind profiler radars in Guangdong Province, deployed at Chaozhou, Luogang, Zengcheng, Huadu, Conghua, Hailingdao, Zhuhai, and Xinhui. The instrument deployed at Luogang utilizes PA band, while the rest utilize LC band. Moreover, Luogang station data are interpolated to get 5-minute temporal resolution to be consistent with the temporal resolution of the LC band. Observations from 2550 high-density automatic weather stations in 2019 in Guangdong Province with 5-minute temporal resolution, including meteorological variables such as surface air temperature, air pressure, wind speed, wind direction, precipitation, etc. Locations of wind profiler radar, automatic weather stations and the distribution of urban impermeable subsurface are shown in Figure 1. The





fifth-generation reanalysis dataset published by the European Centre for Medium-Range Weather Forecasts (ERA5) is used in this study to analyse Convective Available Potential Energy (CAPE) water vapor transport and weather backgrounds for diagnosis of water vapor conditions.



100 Figure 1: The distribution of wind profiler radars and high-density automatic weather stations in Guangdong Province is shown below. Red areas indicate urban subsurface areas (UISA). The locations of the wind profile radar stations are Hailing Island (HLD), Xinhui (XH), Zhuhai (ZH), Huadu (HD), Luogang (LG), Conghua (CH), Zengcheng (ZC) and Chaozhou (CZ).

2.2 Definition of the WSHR

WSHR is defined as follows (Liu et al., 2019): (1) Excluding typhoon-influenced precipitation; (2) Daily precipitation of at least 50 mm is recorded at three or more neighboring stations (spaced ≤ 150 km apart); (3) At least one consecutive 3-hour period with precipitation of at least 5 mm and at least one consecutive 3-hour period with rainfall of at least 30 mm recorded at each station. WSHR events mostly occur under weak synoptic-scale forcing. Therefore, the condition that the precipitation is greater than 200 km away from the front must be satisfied for the WSHR. Eight WSHR events occurring in 2019 are selected according to these definitions.

2.3 Indices and Dynamical Calculations

The physical mechanisms that trigger WSHR events can be ascribed to three mechanisms that characterize the torrential rainfall. The first mechanism is associated with thermodynamic instabilities, which can be identified using the BLH and the





Atmospheric Lifting Index (ALI). The second is related to the dynamical processes identified using the ALI and VWS. In addition, we utilized the Integrated Water Vapor Transport (IVT) to determine the magnitude and direction of moisture transport. The wind profiler radar closest to the automatic stations recording the highest precipitation is chosen as the representative station to calculate atmospheric indices as precursor signals.

2.3.1 Low-Level Jet Index (LLJI)

To quantitatively study the relationship between small-scale fluctuations in the LLJ and heavy rainfall, the LLJI is defined as (Liu et al., 2003):

$$I = \frac{V}{D},\tag{1}$$

where V is the maximum wind speed under 2 km altitude and D is the lowest position of the 12 m s⁻¹ wind speed in a given time period. The downward transmission of the LLJ and the increase in wind speed leads to an increase in I.

125 2.3.2 Vertical Wind Shear (VWS)

130

The VWS of the horizontal wind is conducive to the baroclinic updraft within the convective system, thereby allowing the hydrometeors in the updraft to separate from the updraft. This process prevents the weakening of the updraft buoyancy due to drag effects. Strong VWS has been shown to enhance the entrainment of dry cold air into the middle layer, strengthen the downdraft in the storm, and the cold outflow near the ground. This has the effect of forcing the warm, moist air flowing in to rise more intensely through forced uplifting. The result is an enhancement of convection and a facilitation of the coexistence of the updraft and downdraft for a considerable period of time. The intensity of the VWS has a significant impact on the organizational structure of the convective storm (single cell, multi cell and super cell). WSHR is closely related to the structure, organization and propagation of the mesoscale convective system (MCS), (Chen and Zhang, 2021) Therefore, VWS is selected as one of the precursor signals of precipitation. The following shows the formula of the VWS:

135
$$\Delta V = \frac{\sqrt{(U_{z1} - U_{z2})^2 + (V_{z1} - V_{z2})^2}}{(z_1 - z_2)},$$
 (2)

where ΔV stands for the VWS (units: 10⁻³ s⁻¹), U_{z1} and U_{z2} represent zonal winds at heights z_1 and z_2 , respectively, while V_{z1} and V_{z2} denote meridional winds at the top height z_1 and the bottom height z_2 .

2.3.3 Atmospheric Lifting Intensity (ALI)

It is well established that strong air uplift movements usually precede the precipitation onset. The product of the maximum uplift velocity and the thickness of the uplift layer is therefore calculated to quantify the intensity of the uplift N:

$$N = W_{max} * H * 10, \tag{3}$$



150

155

165



where H represents the atmospheric uplift interval within 0-6 km altitude, when upward vertical velocity occurs in three consecutive observation altitudes; W_{max} represents the maximum vertical velocity of the atmospheric updraft interval.

145 2.3.4 Boundary Layer Height (BLH)

The Boundary Layer Height (BLH) is a pivotal variable to describe the structure of the boundary layer (Seibert et al., 2000), and it is crucial for elucidating turbulent motion. Furthermore, studies have demonstrated that wind speed is an important factor affecting the change of BLH (Li et al., 2024a). As a result, the height of the boundary layer is chosen as an early indicator. Both computational models and experimental findings have shown that the vertical distribution of the refractive index structure parameter, (C_n^2) peaks at the bottom of the top-covered inversion layer; this is where the humidity gradient is significant (Angevine).(Angevine et al., 1994). As Burk (1980) demonstrated, the method is employed to estimate the altitude of the top of the boundary layer. However, it is important to note that there is presence of clouds prior to the onset of precipitation, causing strong turbulent mixing in the clouds and entrainment mixing near cloud boundaries, resulting in higher C_n^2 than that at the top of the boundary layer. Furthermore, entrainment mixing in proximity to the cloud boundary has been observed to result in the occurrence of the peak of C_n^2 within the cloud. Therefore, it can be concluded that the joint use of the peak C_n^2 and the vertical wind speed variance σ_w^2 to estimate the BLH can improve the accuracy in the presence of clouds (Heo et al., 2003). In the mixed boundary layer, the heat flux exhibits a linear decrease in height from the ground to the upper boundary layer limit, reaching a minimum at the upper boundary layer. The vertical heat flux profile demonstrates a correlation with the standard deviation of the vertical velocity, which can be shown as:

$$160 \quad \frac{\sigma_w^3}{z} \approx \alpha^{\frac{2}{3}} * \frac{g}{\theta} * \left(\overrightarrow{w'\theta_v} \right), \tag{4}$$

where σ_w^2 , z, and α denote the turbulent vertical velocity standard deviation, height, and generic constant ($\alpha = 1.4$), respectively, and $\frac{g}{\theta}(\overrightarrow{w'\theta'_v})$ denotes the local buoyancy term, where g, θ , θ , and $\overrightarrow{w'}$ are the gravitational acceleration, the potential temperature, the virtual potential temperature, and the perturbed vertical velocity, respectively. It can thus be concluded that there is a relationship between the profile of the standard deviation of the vertical velocity and the profile of the atmospheric boundary layer sensible heat flux. The primary and secondary peaks are firstly selected in each C_n^2 vertical contour and the height of the peak near the ground surface is chosen as the estimated boundary layer height Z_1 following the relationship above; secondly, a linear regression line of Equation (4) is obtained by least-squares fitting of the previously estimated Z_1 and Z_2 . Finally, the height of the zero value of the heat flux, Z_2 , is estimated by extrapolating the regression line, and the height of the peak Z_n^2 closest to Z_2 is taken as the BLH.

170 2.3.5 Calculation of vorticity and divergence

Based on the 'triangle method (Bellamy, 1949)', the atmospheric vorticity and divergence can be calculated by using three wind profile radar stations deployed into a triangular shape (Wu et al., 2023). The component of each side of the triangle in





the spherical coordinate system is calculated based on the latitude, longitude and earth radius at each vertex position of the triangle (Δx_i , Δy_i , i = 1,2,3). The divergence (D) (unit: s⁻¹) and vorticity (ξ) (unit: s⁻¹) can then be calculated at the same altitude by using the horizontal winds measured at the vertices ($u_i, v_i, i = 1,2,3$). The formulae are as follows:

$$D = \frac{(u_2 - u_1)(\Delta y_3 - \Delta y_1) - (u_3 - u_1)(\Delta y_2 - \Delta y_1) + (\Delta x_2 - \Delta x_1)(v_3 - v_1) - (\Delta x_3 - \Delta x_1)(v_2 - v_1)}{(\Delta x_2 - \Delta x_1)(\Delta y_3 - \Delta y_1) - (\Delta x_3 - \Delta x_1)(\Delta y_2 - \Delta y_1)},$$
(5)

$$\xi = \frac{(v_2 - v_1)(\Delta y_3 - \Delta y_1) - (v_3 - v_1)(\Delta y_2 - \Delta y_1) + (\Delta x_2 - \Delta x_1)(u_3 - u_1) - (\Delta x_3 - \Delta x_1)(u_2 - u_1)}{(\Delta x_2 - \Delta x_1)(\Delta y_3 - \Delta y_1) - (\Delta x_3 - \Delta x_1)(\Delta y_2 - \Delta y_1)},$$
 (6)

2.3.6 Moisture transport calculation and diagnosis of vertical profiles

Moisture transport is one of the most important proxies to characterize the dynamic moisture processes to form precipitation.

180 In this study, we utilized ERA5 data to calculate the IVT from 850 hPa to 1,000 hPa using Eulerian framework.

$$IVT_u = \frac{1}{g} \int_{1000 \, hPa}^{850 \, hPa} qu \, dp \,, \tag{7}$$

$$IVT_{v} = \frac{1}{a} \int_{1000 \, hPa}^{850 \, hPa} qv \, dp \,, \tag{8}$$

$$IVT = \sqrt{IVT_u^2 + IVT_v^2} \,, (9)$$

where the IVT_u (IVT_v) are zonal (meridional) component of the moisture transport vector in kg m⁻¹ s⁻¹, IVT is the magnitude of the vector, g is gravitational accelerations in m s⁻², u and v are zonal and meridional components of the layer-mean wind speed, respectively, q is the layer-mean specific humidity in kg kg⁻¹, and dp is pressure difference between two neighboring pressure levels. Positive values of IVT_u (IVT_v) indicate eastward (northward) zonal (meridional) components.

190 In addition, vertical profiles of moisture transport are characterized by each unintegrated term in Eq (7) for diagnosis in horizontal and vertical components for cross-section analysis of moisture transport and moisture transport diagnosis:

$$VT_u = \frac{1}{g} \int_{p_b}^{p_t} qu \, dp \,, \tag{10}$$

$$VT_{v} = \frac{1}{g} \int_{p_{b}}^{p_{t}} qv \, dp \,, \tag{11}$$

$$VT_{w} = \frac{1}{g} \int_{p_{b}}^{p_{t}} qw \, dp \,, \tag{12}$$

195
$$-m = \frac{\partial q}{\partial t} + \nabla \cdot (VT_u, VT_v) + \frac{\partial \omega q}{\partial p}, \tag{13}$$



205

210



where $VT_{u/v/w}$ are three components of moisture transport in each vertical layer in kg m⁻¹ s⁻¹, p_t and p_b are top and bottom layers of each ERA5 vertical layer ($p_t \ge 500$ hPa and $p_b \le 1,000$ hPa), w is vertical components of velocity in m s⁻². m represents condensation rate at specific grid in three-dimensional space (time, latitude and longitude) related to precipitation rate, which consists of local rate of change of moisture $\frac{\partial q}{\partial t}$, divergence of moisture transport $\nabla \cdot (VT_u, VT_v)$ and vertical moisture transport term $\frac{\partial \omega q}{\partial p}$. Meanwhile, we used Convective Available Potential Energy (CAPE) in ERA5 (unit: J) to study convection.

3 Overview of WSHR

We found eight WSHR events from April to July, 2019 in Guangdong Province following the WSHR definitions. Table 1 shows the times of precipitation onset and the maximum hourly precipitation for each of the eight cases (all times are in UTC). Figure 2 shows the distribution of daily precipitation observed by high-density automatic weather stations for each case. Figure 3 shows the daily mean precipitation calculated from all cases. The WSHR is mainly concentrated in three areas: the vicinity of Hailing Island in western Guangdong (hereafter the western region), the Pearl River Delta urban agglomeration area (the central region), and the Chaozhou area in eastern Guangdong (the eastern region). The Pearl River Delta urban agglomeration region experienced the highest cumulative precipitation levels, particularly in the vicinity of the Greater Bay Area.

Table 1: General overview of eight WSHR events.

	0413	0418	0420	0526
Start time(UTC)	05:50	09:45	03:30	01:00
Radar stations	HLD	ZH	LG	CZ
Max Rainfall intensity(mm/h)	21.9	9.6	14.5	13.9
Region	Western	Central	Central	Eastern
	0529	0610	0624	0710
Start time(UTC)	18:40	07:35	01:45	21:00
Radar stations	HLD	HD	ZC	CZ
Max rainfall intensity(mm/h)	10.4	10.6	7.9	6.8
Region	Western	Central	Central	Eastern





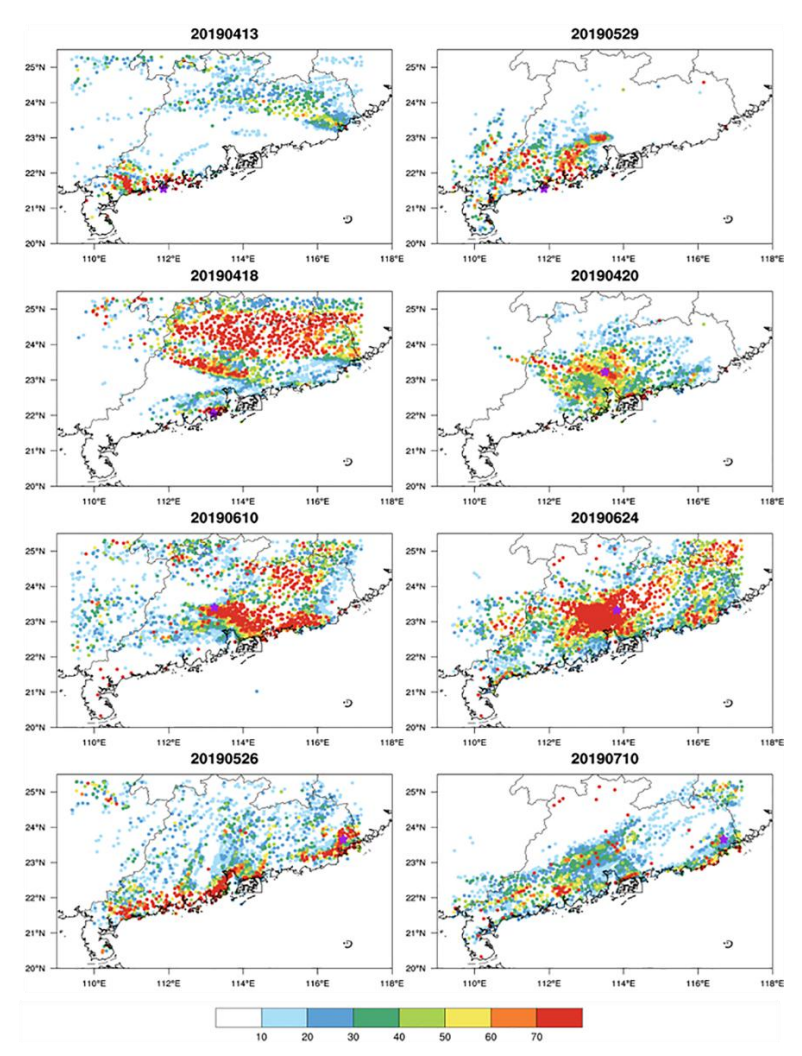


Figure 2: Rainfall distribution of individual WSHR cases in 2019 (unit: mm d⁻¹).

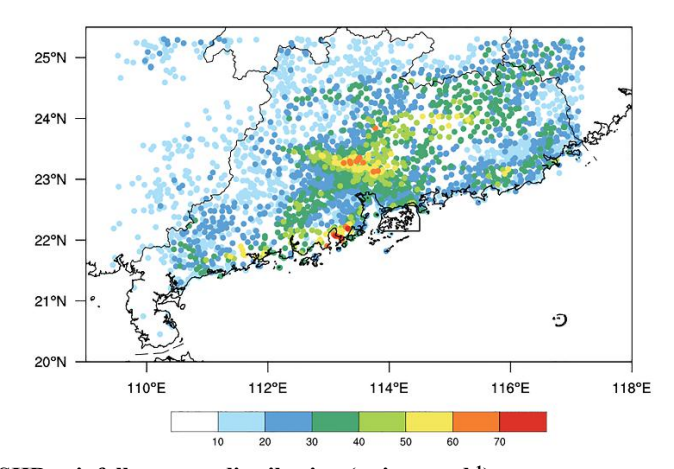


Figure 3: Composite mean of WSHR rainfall amount distribution (unit: mm d-1).





Figure 4 and Figure 5 show synoptic conditions at lower levels for each case of the WSHR. Western region events are dominated by high pressure system or without weather systems, with mild southerly wind. The synoptic conditions in the central and eastern regions exhibit significant similarities, characterized by a low-pressure system in northwestern South China, accompanied by the edges of a subtropical high in the eastern areas, as well as the presence of monsoon troughs and convergence zones. These WSHR events in two regions are dominated by southerly or southwesterly with high wind speed, with jet streams at 850 hPa and 925 hPa. Southerly prevails in South China in April to May, and southwesterly prevails in June to July.

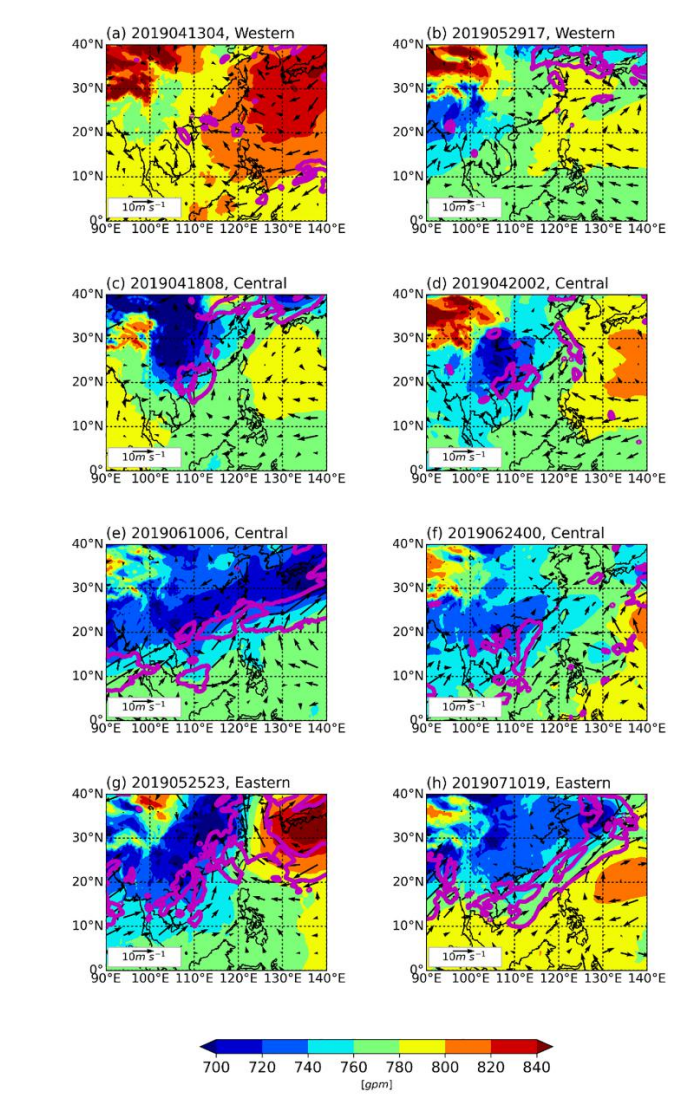


Figure 4: Synoptic scale analysis of eight WSHR events at 850 hPa. (a-b) WSHR events in the western region; (c-f) central region and (g-h) eastern region. Geopotential heights in gpm, wind vectors (black arrows) in m s⁻¹ with wind speed over 10 m s⁻¹ marked in magenta contours.

225





235

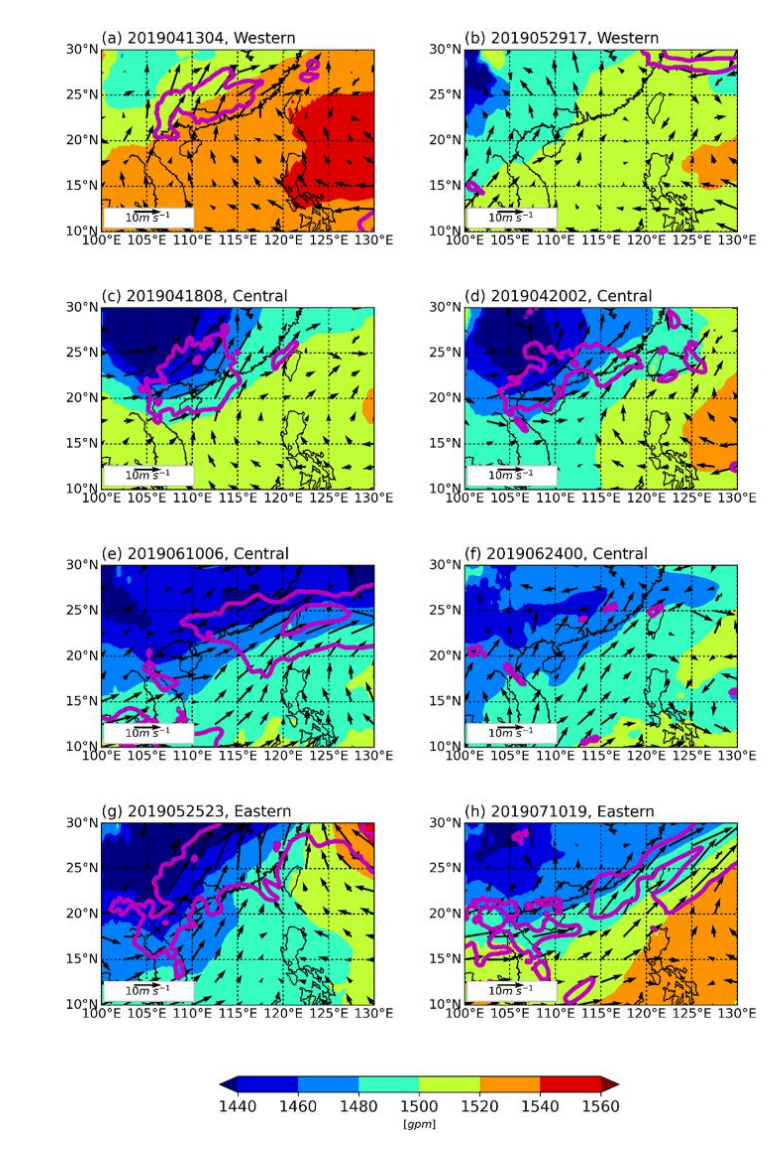


Figure 5: Same as Figure 4, but at 925 hPa.

Figure 6 shows time-altitude diagram of wind field and vertical motions of each representative station, while Figure 7 shows VWS mean 3 earlier the onset of the WSHR. Substantial vertical motions are observed within the lowest 6 km of altitude, indicating robust convection. Subsidence prevails hours before the onset, while the vertical motions reversed during and after the onset. Vertical profiles in the western region (Figure 6a, b) shows prevailing southerly below 2 km before the onset of WSHR, and westerly at 3 km and above. Clockwise turning of wind direction with height implies the existence of warm advection in the western region. Wind speed above 2 km significantly increases and turns clockwise with increasing height



245

250



as local convection develops. There is deflection in wind speed below 2 km with the start of precipitation. The VWS increases where wind speed direction changes significantly (Figure 7a, b). There is strong westerly with the maximum wind speed 18 m s⁻¹ over Pearl River Delta, whose vertical profile of horizontal wind show that the strongest jet stream is at 4 km before the onset of precipitation. The strongest wind in the jet is 12 m s⁻¹ located at 1–2 km. The altitude of jet maximum decrease before the onset of the WSHR, consistent with previous studies (Li et al., 2024). The wind shear diagram shows large VWS values at 1–2 km and 4 km, implying strong VWS at jet streams. There is sharp decrease in wind speed below 1 km due to larger friction at urban regions. Wind speed and direction wiggle significantly close to the onset of the WSHR events. The LLJ is located below 2 km and wind directions are homogeneous above 1 km before the onset of WSHR events in the eastern region.

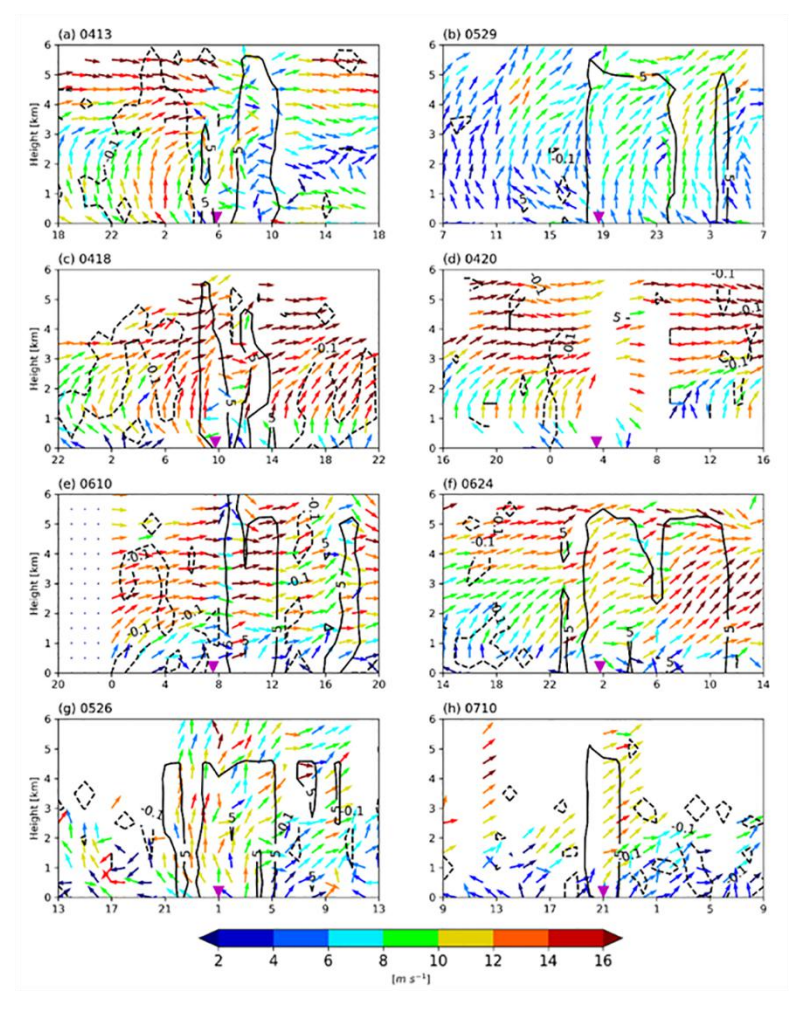


Figure 6: Time-altitude diagrams of horizontal wind for each ease. Vectors represent wind speed in m s⁻¹, dashed lines show the contour of -0.1 m s⁻¹ of vertical wind speed, the solid shows 5 m s ⁻¹, triangles mark the onset of WSHR events.





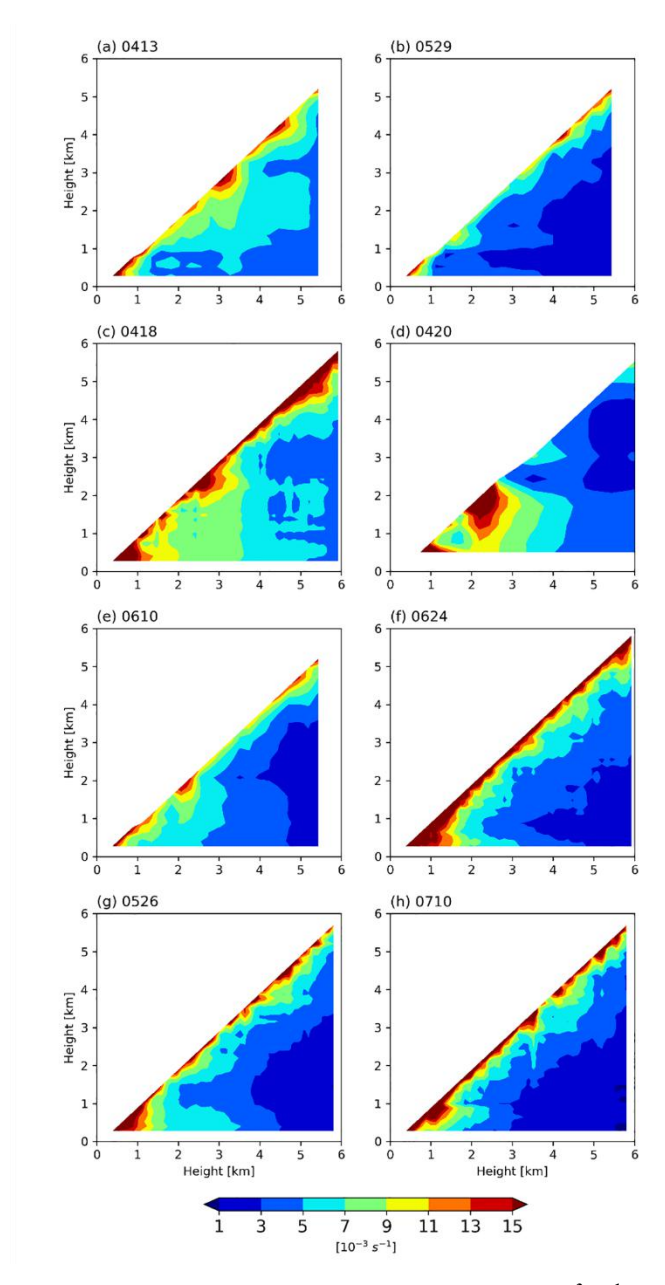


Figure 7: 3-hour mean VWS before the onset of precipitation for each case (unit: 10^{-3} s $^{-1}$). x axis represents high altitude, y axis represents low altitude.

There are significant fluctuations of the horizontal wind speed and direction along vertical dimension through the all cases. The statistical analysis of dynamics prior to the onset of precipitation is conducive to identifying the characteristics of dynamic factors and detecting precursor signals.





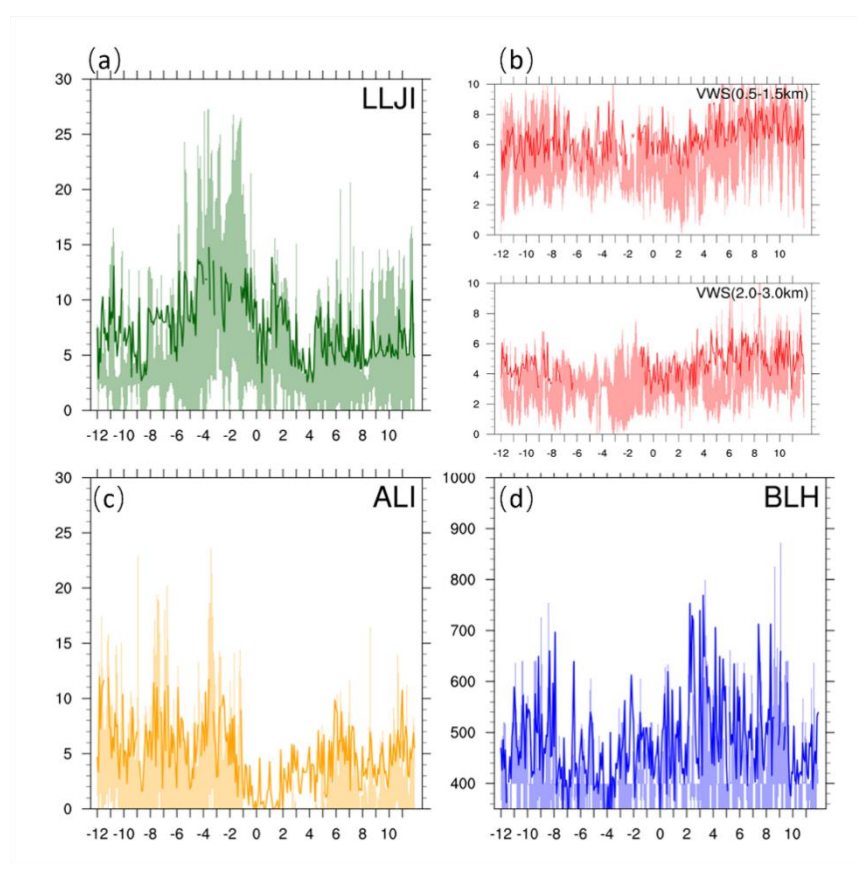
260 4 Results

265

270

4.1 Indices and Dynamical Calculations

We standardized the onset of the WSHR events for each case to compute composites of LLJI, VWS, ALI and BLH indices from 12 hours before the onset to 12 hours after the onset (Figure 8). Results show that peak values of LLJI and ALI are observed 4 hours before the precipitation with consistent changes, implying the sudden increased instability into the boundary layer and upper atmosphere, with a sudden change of the wind speed paired with a more intense convection. The VWS attains maximum values within 0–1 km and 2–3 km, as showed in Figure 7 and into Supplementary Figure S1. (supplementary materials). Therefore, we computed the VWS at 0.5–1.5 km and 2–3 km, respectively. Stronger VWS is observed at 0.5–1.5 km, implying significant change in wind speed and direction at 0.5–1.5 km. The BLH first increase and then decrease over the last 4 hours before the onset of the WSHR. The changes of these four indices revealed the atmospheric dynamical processes before the onset of WSHR that atmosphere becomes unstable before the onset of WSHR, that the LLJ strengthens and that the lifting activities are strong. These indices are of great importance to precipitation prediction and analysis.





285

290



Figure 8: Temporal evolutions of (a) LLJI (unit: 10⁻³ s ⁻¹), (b) VWS (0.5–1.5km, 2–3km, unit: 10⁻³ s ⁻¹), (c)ALI (unit: 10⁻³ m² s ⁻¹) and (d)BLH (unit: m). x axes are in hours. The onset of the WSHR events is normalized as "0" and the time before the WSHR are labeled as negative numbers. Solid lines represent mean values. Shadows represent 25 %–75 % quantile.

4.2 Spatiotemporal characteristics of precursor signals

4.2.1 Summer monsoons over the South China Sea

Moisture sources of WSHR events are Indian Ocean, western North Pacific and the South China Sea, which affects the spatial distribution of heavy rainfall with varying moisture transport paths (Ning et al., 2023). South China is deeply affected by the monsoon system, which is highly associated with moisture transport paths.

The 2019 South China Sea monsoon broke out in the 2nd pentad in May (National Climate Centre (NCC, http://www.ncc-cma.net), and precipitation is mainly concentrated in the Pearl River Delta (PRD) region and the west coast of Guangdong before the monsoon onset, while the frequency of precipitation in eastern Guangdong increased significantly after the monsoon onset over the South China Sea. When comparing the cases in Yangjiang during pre-monsoon and post-monsoon period (Figure 9), there are distinct variations of the BLH before heavy precipitation events, regardless of the monsoon phase. Results show that LLJI, WVS and ALI are higher than that before the monsoon onset, with sharp decrease in WVS at 0.5–1.5 km. The pre-monsoon cases (blue line) show lower mean BLH with larger oscillation amplitudes, whereas the post-monsoon cases (red line) show higher mean BLH with reduced variability, which is likely due to instability of atmosphere before the monsoon onset and stark contrast of wind fields at different heights. Moreover, consistent wind field at different heights during post-monsoon period and persistent warm, moisture transport are also the reasons why post-monsoon cases show higher mean BLH. Four indices show that there is significant difference in atmospheric conditions to form heavy rainfall between pre-monsoon and post-monsoon season over the western coastal regions.



305



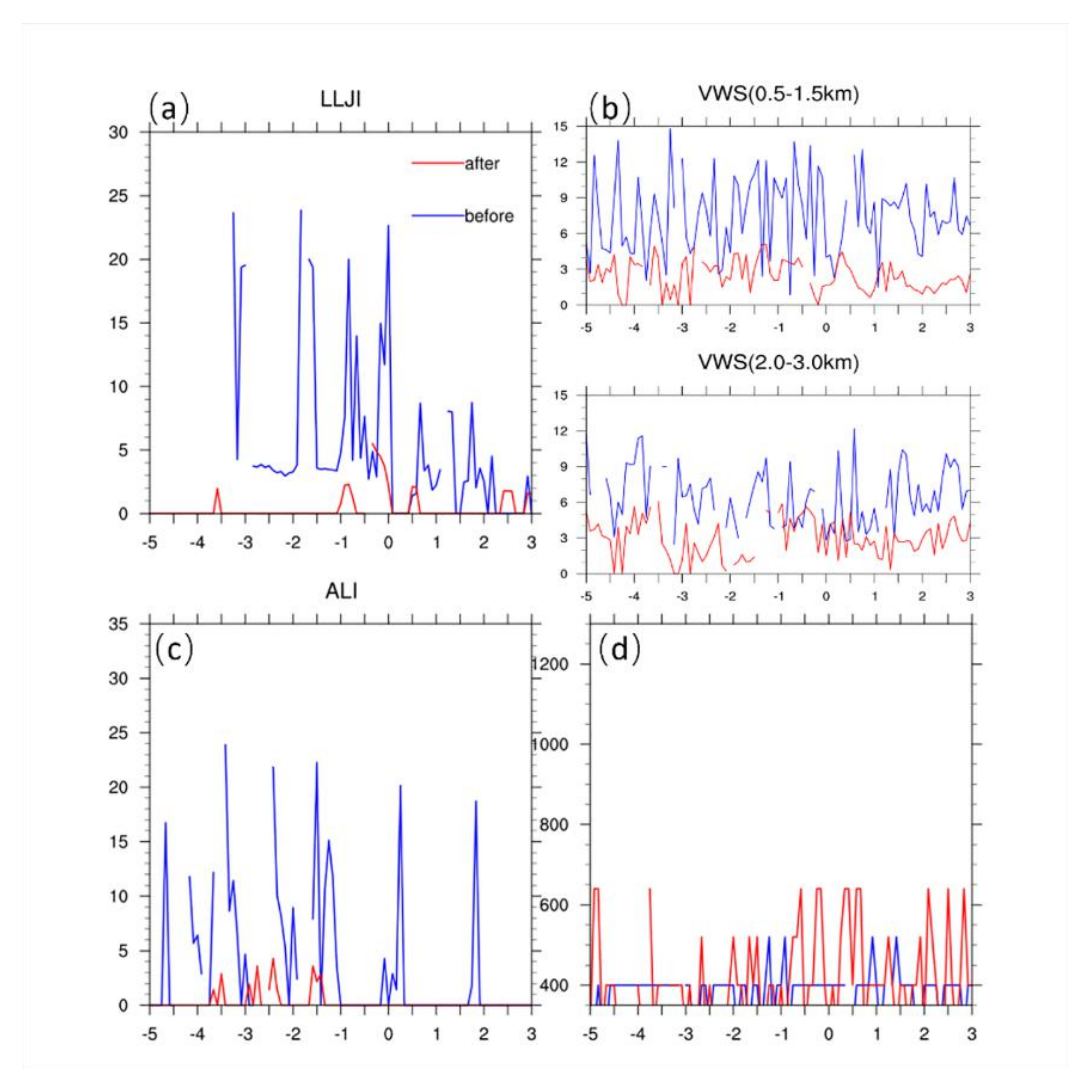


Figure 9: Temporal evolution of (a) LLJI (unit: 10⁻³ s ⁻¹), (b)VWS (0.5-1.5km, 2-3km, unit: 10⁻³ s ⁻¹), (c)ALI(unit: 10⁻³ m² s ⁻¹), (d)BLH (unit: m) before (red) and after (blue) the monsoon onset. X axis represents hours away from the onset of the WSHR events (marked as "0"). The time before the onset is marked as negative numbers.

The composite mean IVT below 850 hPa 2 hours before the onset of WSHR and equivalent potential temperature are shown in Figure 10. Moisture is mainly distributed over northern South China Sea and coastal regions in Guangdong Province before monsoon onset, where southwesterly from Indian Ocean and southeasterly under the effect of the subtropical high converge, resulting in large LLJI, VWS and ALI over the western region. Monsoon onset results in increase of moisture from the Bay of Bengal and western Pacific Ocean, the retreat of the subtropical high and the northward shift of the LLJ, which fosters moisture transport to reach deep inland. There is increase in the WSHR events over the eastern region after the monsoon onset. There are no dominating weather systems over the western region with weak dynamical effects, but with higher BLH after monsoon onset due to increased sea surface temperature. Overall, the fluctuations and trends of indices are





more complex before monsoon onset, implying interactions of multiple atmospheric conditions under unstable atmosphere, resulting in torrential rainfall. The LLJ shifts northward with steady southwesterly after monsoon onset, when the precipitation area and mechanisms are quite different from that before monsoon onset.

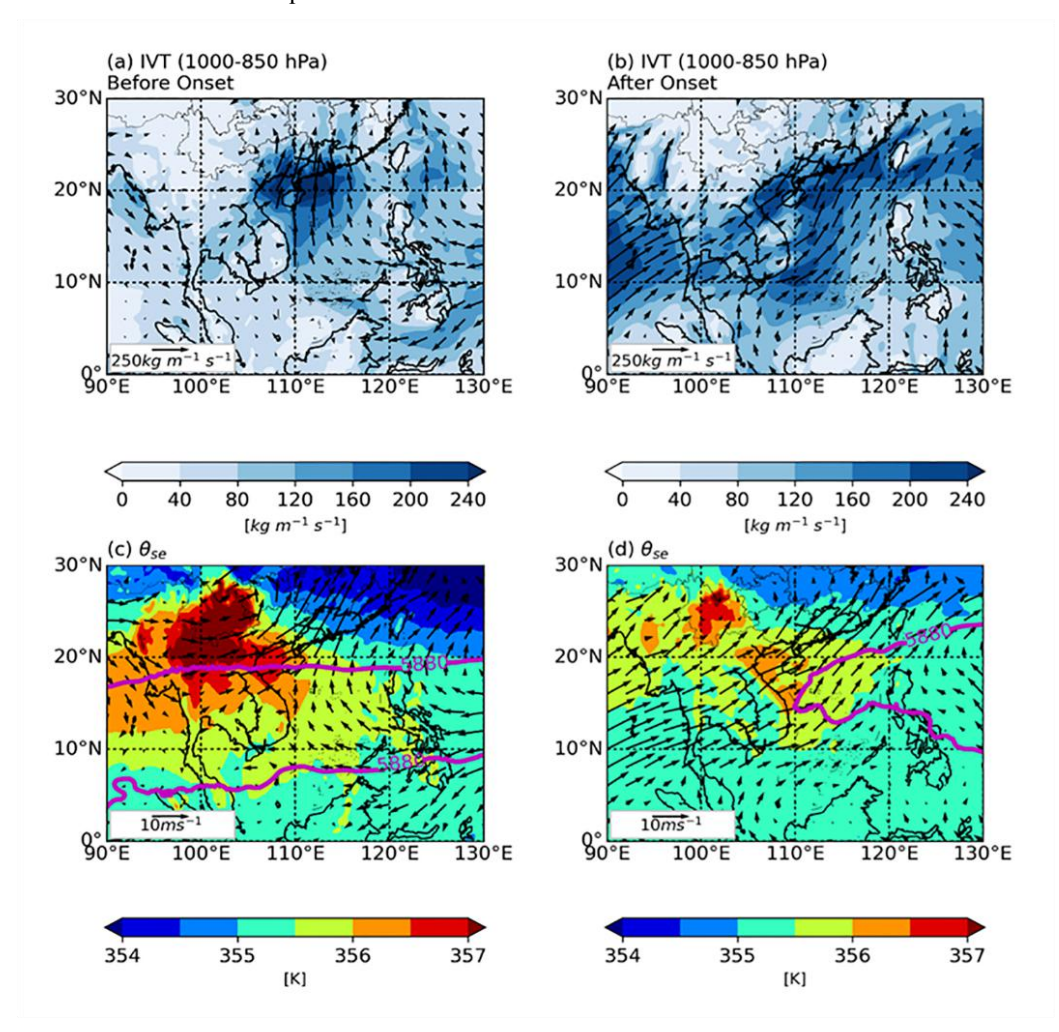


Figure 10: (a, b) the IVT from 1000 hPa to 850 hPa (unit: kg m⁻¹ s⁻¹); (c, d) equivalent potential temperature (unit: K) (a, b) before and (c, d) after the monsoon onset.

4.2.2 Geographical conditions

The composite mean time series of LLJI, VWS, ALI and BLH before and after the onset of WSHR events are shown in Figure 11. Discontinuous peak values of LLJI are observed 3 hours before the onset of WSHR events. Initially, the LLJI over the central region exhibits an increase followed by a decrease three hours prior to the onset of WSHR events. This increase-decrease pattern constitutes a significant feature for precipitation nowcasting. During the same period, the LLJI





remains considerable over the eastern region, indicating the persistence of the LLJ. VWS values are about the same at 0.5–1 km and 2–3 km 3 hours before the onset, but with significant decrease in WVS 2 hours before the onset. Large VWS values are observed at 0.5–1.5 km over central regions, implying the effect of surface friction resulting in decreased wind speed at the low level. The increase in ALI is observed over western and central regions 3 hours before the onset of the WSHR, implying strong uplift. Maximum mean BLH values are observed over the central region with most significant change, with peak values 2–3 hours before the onset of the WSHR, which is likely the effects of climatological features, terrain and urbanization.

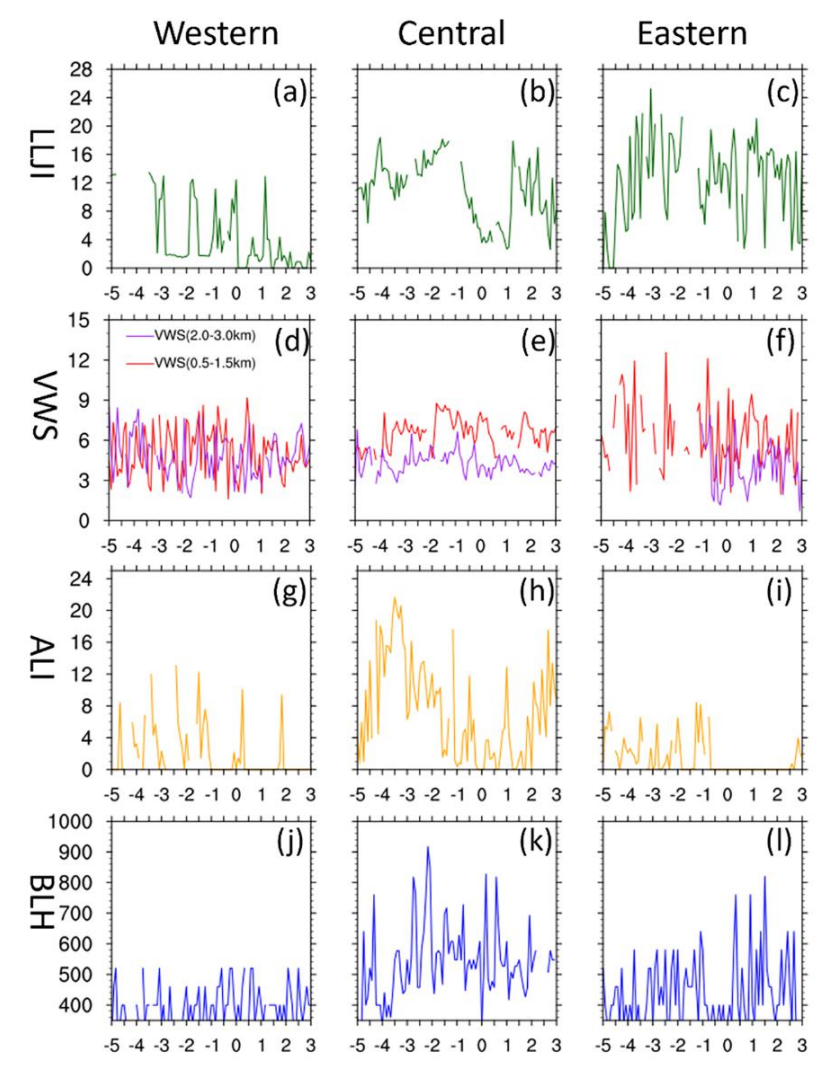


Figure 11: Composite mean temporal evolution of precursor signals of (a–c) LLJI(unit: 10^{-3} s $^{-1}$), (d–f) VWS (0.5–1.5km, 2–3km, unit: 10^{-3} s $^{-1}$), (g–i) ALI (unit: 10^{-3} m² s $^{-1}$) and (j–l) BLH (unit: m) indices over (a,d,g,j) western, (b,e,h,k) central and (c,f,i,l) eastern regions. The onset time is normalized to "0", before which is labeled as negatives.

325



335

340

345



To investigate the relationship between precursor signals and precipitation in different regions, a sliding window correlation (SWC) analysis is performed (Figure 12). In the western region, significant positive correlations are found between both the ALI and VWS with precipitation during the 2 h period prior to precipitation onset, showing that strong uplift airflow and LLJ are conductive to form precipitation. Within 30-80 minutes prior to the onset, both LLJI and the VWS (2-3 km) are correlated with precipitation, which is likely associated with increase of the LLJ prior to precipitation. The ALI observed 30 minutes before the precipitation onset exhibits a positive correlation with precipitation, suggesting that a strong updraft is conducive to precipitation formation. BLH, LLJI and VWS 2-3 hours prior to the onset are positively correlated with precipitation over the central region, implying that higher BLH and stronger LLJ are conductive to heavy rainfall. BLH, ALI, LLJI and VWS at 90 minutes prior to the onset, which is the turning point to trigger the WSHR, are negatively correlated with precipitation. Moreover, convergence of wind speed, weaker VWS, inhibited lifting and lower BLH are observed 90 minutes prior to the onset. In the eastern region, the VWS within 0.5-1.5 km range and the ALI index measured 60-150 minutes prior to the onset of precipitation are significantly positively correlated with precipitation events. In contrast, LLJI exhibits a weaker positive correlation with precipitation. Overseeing the results above, precipitation over western region is sensitive to the ALI and the LLJI 2-3 hours prior to precipitation. The rainfall over central region is sensitive to the strengthening of BLH, LLJI and VWS 2-3 hours prior to the onset and the weakening of the BLH, LLJI and VWS 30-90 minutes prior to the onset. Precipitation over eastern region is sensitive to the increase of ALI and VWS at 0.5-1.5 km, which are 60–150 minutes prior to the onset.

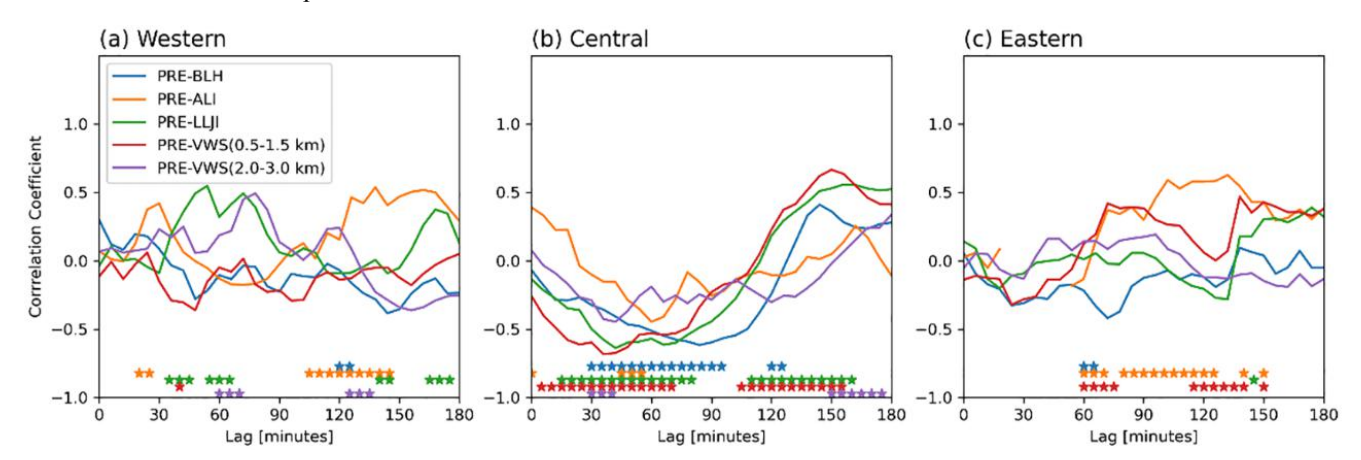


Figure 12. The SWC of precursor signals with precipitation over (a) western, (b) central and (c) eastern region. X axis shows the lag time in minutes. Stars show significance level of 0.05.

To further explore the reasons for this inter-regional signal difference, the water vapor fluxes oner the three regions are compared (Figure 13). In the western region, water vapor is mainly concentrated in the lower 900 hPa, and water vapor is mainly transported from south to north and converges. Vertical integration also confirms that the water vapor converges within the region delimited by 20°N–23°N latitudes. This indicates that this region primarily relies on the influx of low-level



360



warm, moist air and may be susceptible to topographic uplift. Water vapor transport in the central region is concentrated at heights of 900 hPa and 700 hPa, which is consistent with the heights of the double LLJs when combined with the heights of the wind profiles in the previous section. The vertical integration results show that the water vapor flux in this region is most concentrated at 23°–25°N. The water vapor flux in the eastern region is more active in the middle layer (500–700 hPa), and the low-level transport is weaker and more extensive compared to the central region. Upward-pointing vector arrows indicate oblique vapor transport through upper-level systems. Vertical integration reveals intense moisture transport across Guangdong Province, extending northward. This region exhibits the widest extent and the greatest intensity of moisture transport among the three regions, consistent with regulation by circulation at the edge of the Subtropical High or southwest jet streams.

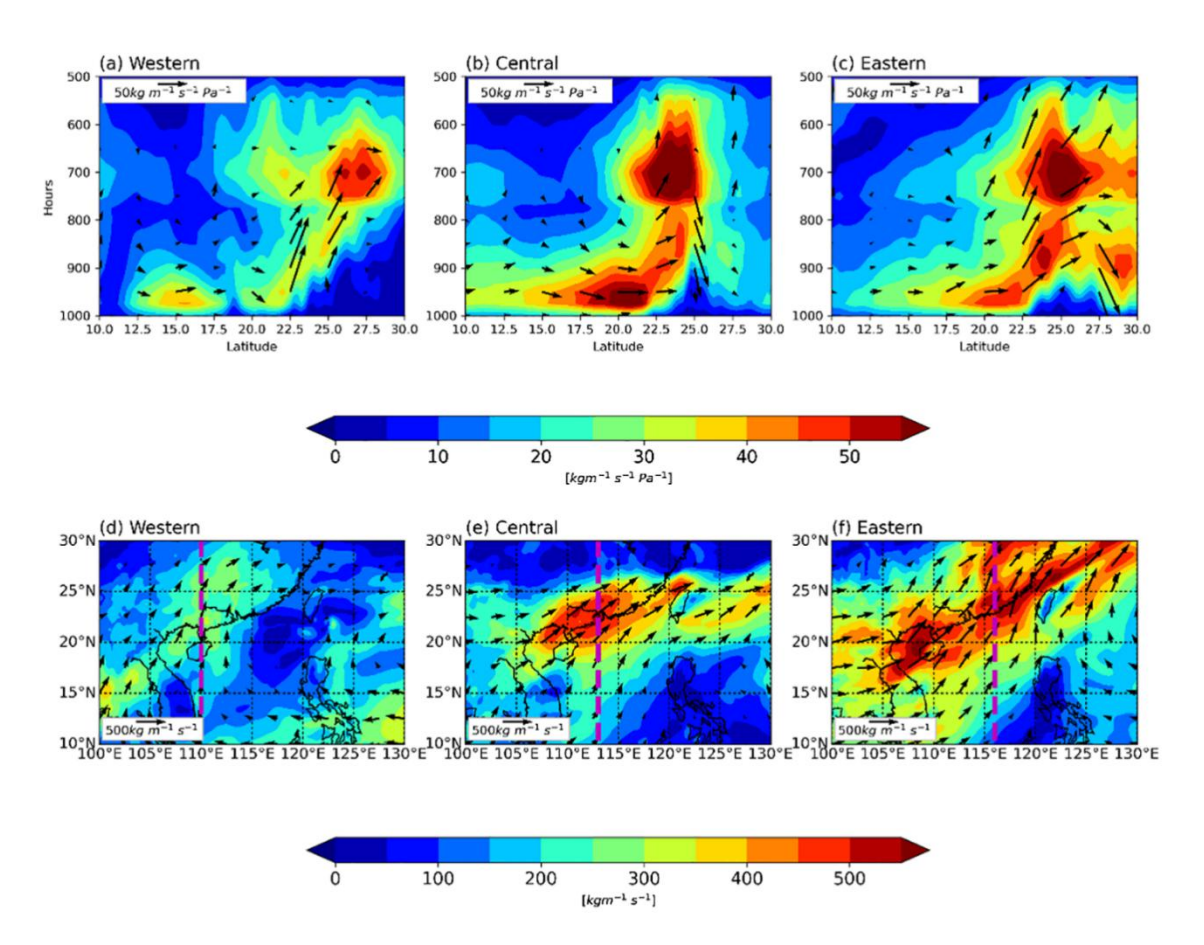


Figure 13. (a) Western region, (b) Central region, (c) Eastern region: Vertical profiles of water vapor flux along the purple line (upper panels) and spatial distribution of vertically integrated water vapor flux (d-f). Arrows represent water vapor vectors. The vertical velocity in the upper panels is magnified by a factor of 50.

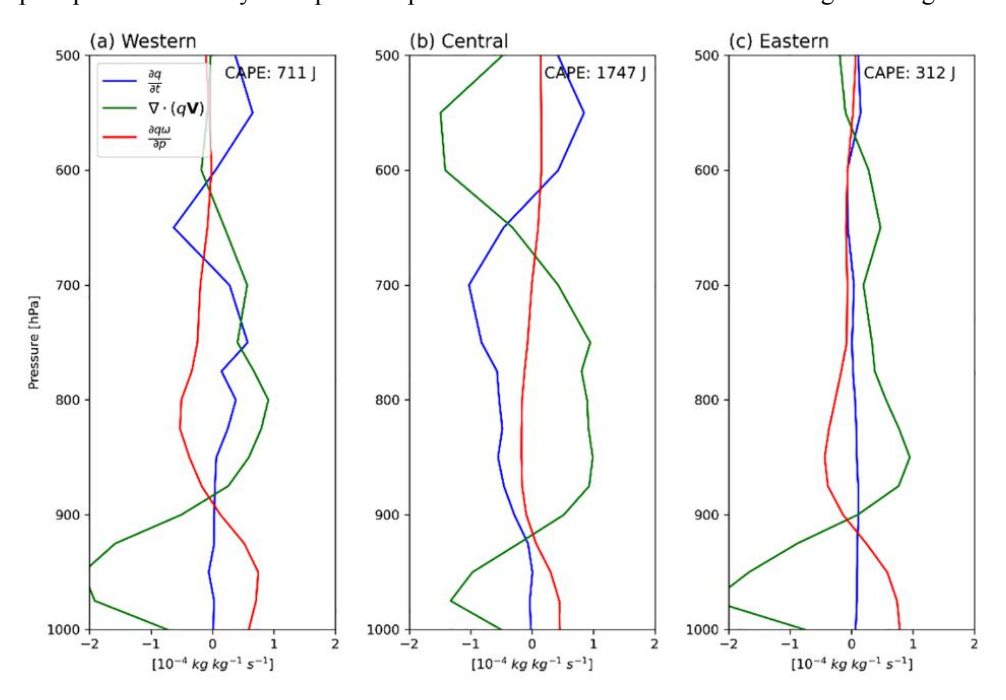


375



As shown in figure 14, in order to further clarify the dominant mechanism of WSHR events in the three regions, typical cases in each region are selected and a power term decomposition is performed at the moment of rainfall onset. The water vapor variability in the western region is positive at 500–700 hPa, indicating water vapor accumulation. The water vapor flux divergence is negative at 900–1000 hPa and positive at 600–900 hPa, with strong convergence in the lower layers and divergence in the middle layers. The upward motion is also stronger from the vertical transport term; water vapor in the central region gradually decreases in the 600–900 hPa interval, with strong convergence in the lower layers and strong radiation in the middle layers. In contrast to the western and eastern coastal regions, there is also a convergence zone at 500–700 hPa, which may be related to the coupling of westerly jet and low-level jets. There is a persistent updraft with the largest CAPE value, indicating stronger convection; the eastern region has less water vapor variability and is positive overall, which combined with the water vapor integral (Figure 13) shows that there is sufficient water vapor. Low-level convergence is strongest, with a consistent divergence zone at 600–900 hPa, which can lead to stronger vertical pumping.

In general, it is evident that there are markedly distinct mechanisms among the three regions. In the western region, precipitation is predominantly initiated by orographic lifting effects associated with 900 hPa level moisture advection that occurs perpendicular to the coastlines with short pathways. Little local moisture over the central region is observed, whose precipitation relies on advective moisture transport in local perspective. Precipitation in the over eastern region mainly relies on moisture transport at 700 hPa under effects of synoptic jet. Paths and height distribution of moisture transport determines the difference of precipitation intensity and spatiotemporal distribution of four indices among three regions.





395



Figure 14. (a) Western region, (b) Central region, (c) Eastern region: Regional average vertical profiles of water vapor budget decomposition terms and CAPE values.

390 4.3 Typical examples of urban agglomerations

The precursor signals of WSHR are classified and compared above, and the characteristics of precursor signal changes under different circumstances are counted. The precursor signals of the wind field over the central region are more complex because they are influenced not only by meteorological factors but also by urban agglomerations. To investigate the differential effects of urban versus rural underlying surfaces on wind field characteristics during WSHR events, a typical example in urban agglomerations on 20 April 2019 is selected to study the characteristics of wind field changes before the occurrence of WSHR in the Pearl River Delta (PRD) urban agglomerations region. According to Figure 1, Luogang station (59287) is selected as an urban station, and Huadu station (59284), Conghua station (59285) and Zengcheng station (59294) are selected as suburban stations.

Precursor signals at Luogang station are stronger than the other stations (see Fig. 15), as Luogang station is located in the city center, thereby more affected by urbanization. Compared with the relatively small LLJI in Conghua area, the changing characteristics of LLJI in Zengcheng and Huadu areas are closer. Figure 15b shows the VWS at the four stations, with a weaker signal in Huadu area, which starts to increase 70 minutes before the precipitation onset, 10–15 minutes slower than the other three areas. The ALI of the four stations shows that the updraft in Luogang area starts to increase significantly 100 minutes before the occurrence of precipitation, earlier than the other three sites. The maximum ALI at Luogang is the largest among the four sites, indicating that the vertical motion of the atmosphere is closely related to the subsurface. There are differences in the changes of BLH before the occurrence of precipitation at the four sites. The BLH in Luogang is significantly higher than all the other sites, with sharp increase at 100 min before precipitation, and gradual decrease at 80 min before precipitation. The BLH in Huadu, Conghua and Zengcheng started to increase 75 min before precipitation, later that in Luogang. The change of BLH in Zengcheng area is the least obvious.





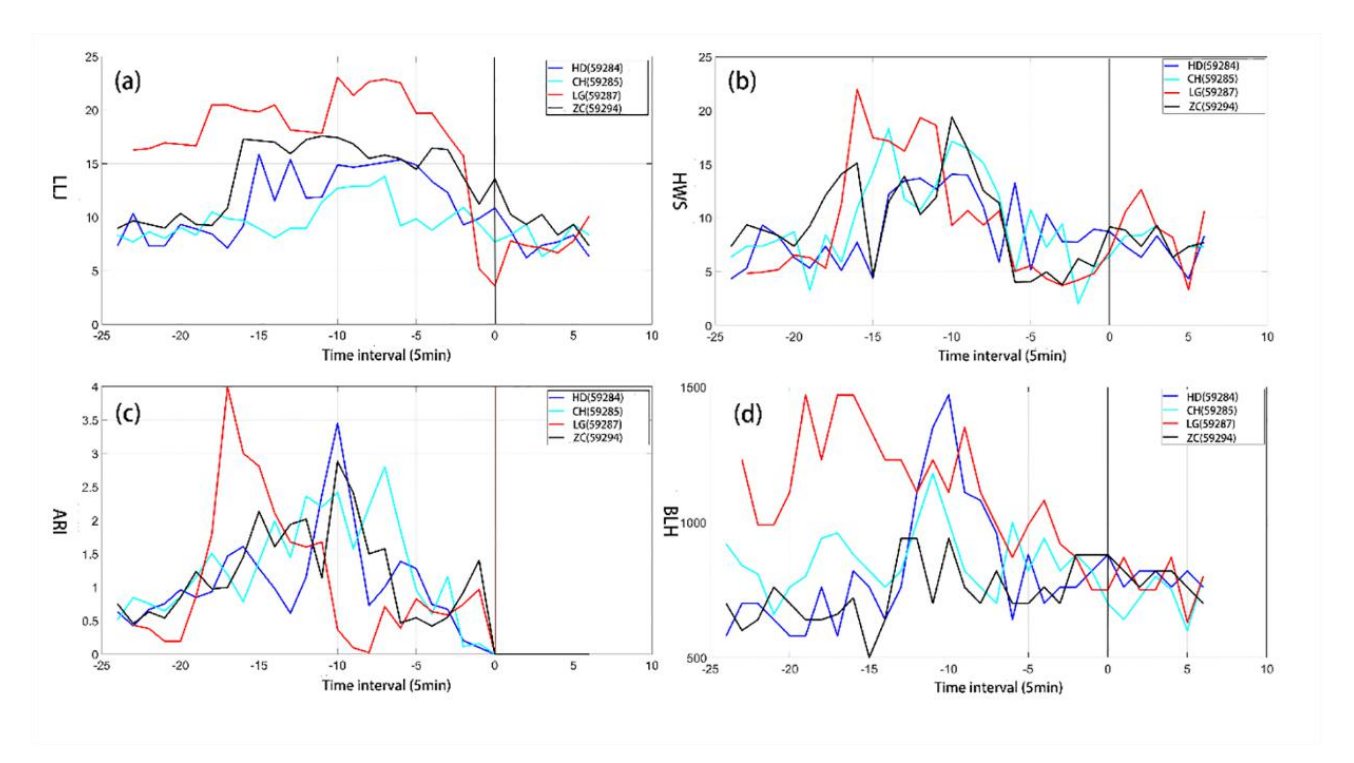


Figure 15. Urban-rural variation of precursor signals for WSHR on April 20. The blue line represents Huadu station, the cyan line represents Conghua station, the red line represents Luogang station, and the black line represents Zengcheng station. (a) Low-level jet index (unit: 10^{-3} s^{-1}); (b) Horizontal wind shear (unit: 10^{-3} s^{-1}); (c) Atmospheric lifting intensity (unit: m km s⁻¹); (d) Boundary layer height (unit: m).

Analyzing the wind profile characteristics of the four stations (Fig. 16), there is a westerly jet stream with wind speed larger than 16 m s⁻¹ above 3km, which is SLJ. There is southerly wind with wind speed larger than 10 m s⁻¹ at 1–2 km, which is BLJ. About 1 hour before rainfall, wind speed decreases at high altitudes and increases at low altitudes. Momentum is transferred from the upper layer to the lower layer, promoting the development of the BLJ. To explore the impact of this wind speed change on VWS, Figure 17 shows 3-hour average diagram of the vertical shear of the horizontal wind before precipitation at four wind profiler radar stations. Strong VWS areas appeared at all four stations before precipitation. The VWS is the strongest below 1 km, indicating that the LLJ in the boundary layer at the lower level is continuously strengthening. The strongest VWS is found at urban station (Fig. 17c).





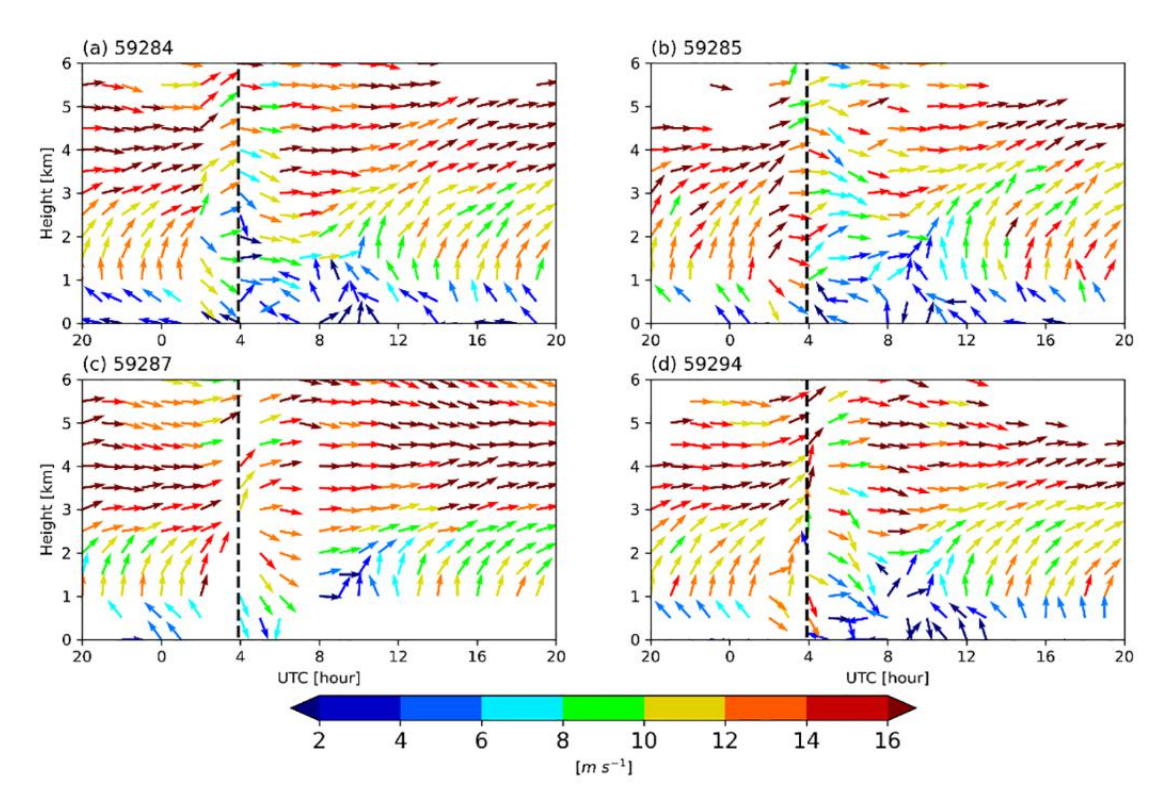


Figure 16. Variation of horizontal wind field on April 20. (a) Huadu station; (b) Conghua station; (c) Luogang station; (d) Zengcheng station (vectors, unit: m s⁻¹, dashed line represents the rainfall onset time).





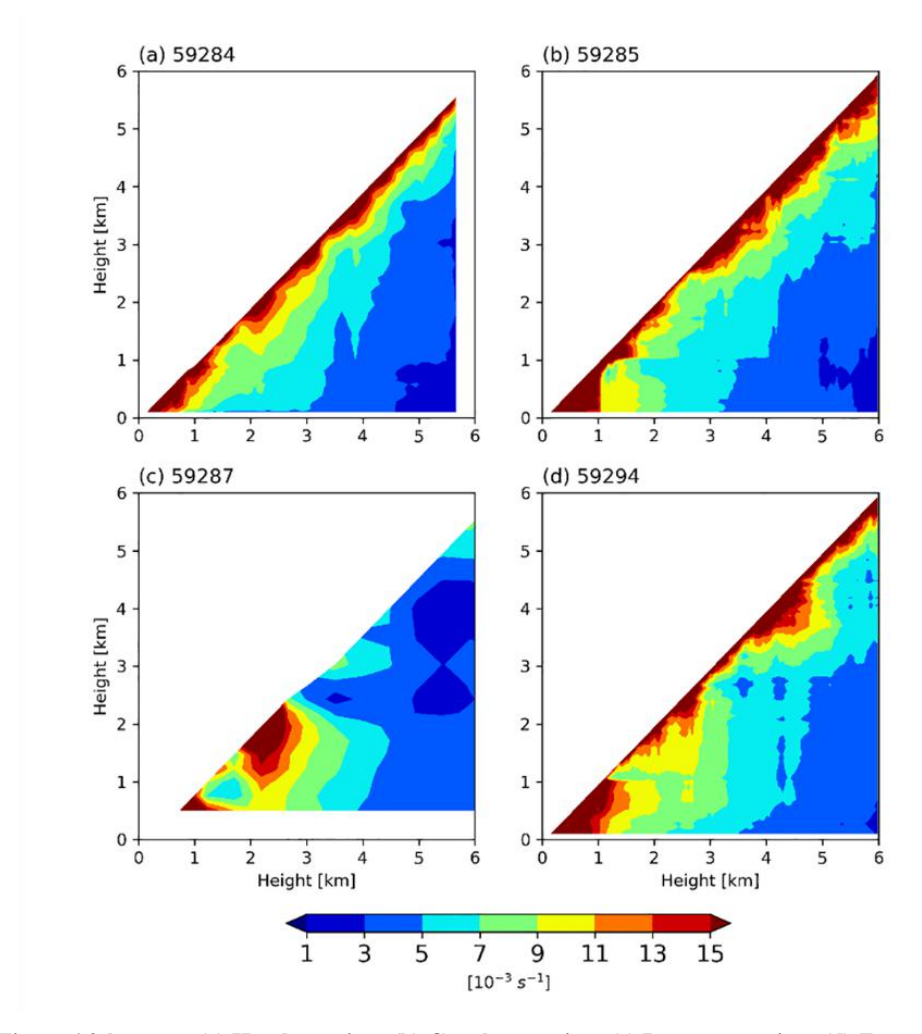


Figure 17. As in Figure 16, here are (a) Huadu station; (b) Conghua station; (c) Luogang station; (d) Zengcheng station.

To further explore the influence of jets on rainfall, the horizontal wind data from four wind profiler radars are used to calculate the vorticity and divergence at 1 km and 4 km, respectively (Fig. 18). Vorticity at 1 km in the suburban area is positive and the divergence is negative 2 hours before the precipitation occurs, indicating that the urban underlying surface in Guangzhou is conducive to the convergence of the offshore BLJ, and a large amount of warm, moist air from the sea converges in the lower layer of the city. The vorticity in the suburban area at 4 km is greater than that in the urban area, and the divergence in the urban area is greater than that in the suburban area, indicating that the wind speed of the SLLJ continues to increase after passing through the urban area. In comparison with suburban areas, urban centers are more conducive to the establishment of a structure characterized by low-level convergence and high-level divergence. Observations of stronger horizontal wind shear and atmospheric uplift can be made in urban areas before precipitation occurs.





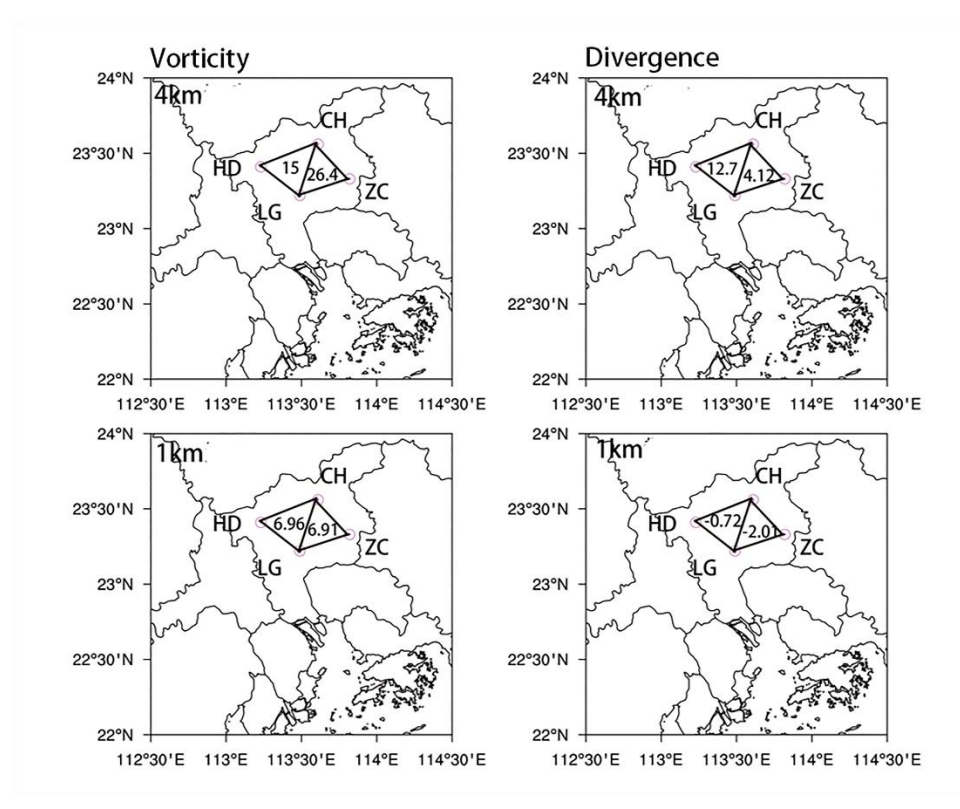


Figure 18. Vorticity (unit: 10^{-5} s⁻¹) and divergence (unit: 10^{-5} s⁻¹) at heights of 1 km and 4 km in the Guangzhou suburban area, 2 hours before precipitation onset. (HD) Huadu station; (CH) Conghua station; (LG) Luogang station; (ZC) Zengcheng station.

5 Discussion

445

450

455

460

5.1 Possible mechanisms of signal differences between regions

In recent years, many studies have investigated into the physical mechanisms of WSHR. Both Yangjiang and Shanwei are coastal areas, but their rainfall characteristics are different. Such difference is associated with dominant weather systems, water vapor and instability conditions, terrain forcing, and land-sea circulation (Chen et al., 2019). The spatial configuration of low-level water vapor transport has an important impact on the cumulative precipitation distribution of extreme mesoscale convective systems (Wang et al., 2025). The synergy of dual low-level jets, orographic lifting, and boundary-layer convergence lines performs a pivotal function in the occurrence of WSHR events (Liang and Gao, 2021; Pu et al., 2022; Zhang et al., 2022b). Moisture transport from the South China Sea to the Shanwei area is crucial for triggering warm-sector rainstorms (Zhong and Chen, 2017). A study of an extreme case in the Guangzhou urban agglomeration (Gao et al., 2021; Huang et al., 2019) found that the urban heat island effect, low-level convergence troughs, topography, and strengthening of low-level southerly winds are the key factors to trigger convection. The precipitation mechanism of WSHR varies spatially,



465

470

475

480



and thus leads to significant inter-regional differences in the characteristics of the dynamical factors, which can be attributed to the characteristics of the three main types of regions: western coast, central urban agglomeration, and eastern coast.

- (1) In the western region, the WSHR is characterized by low-level warm, moist air convergence and orographic uplift. Wind profile analysis shows that southerly winds dominate below 2 km, within 2 hours prior to the heavy rainfall, while westerly winds prevail above 3 km. The clockwise rotation of wind direction reflects the warm advection process. Water vapor transport is mainly concentrated below 700 hPa, which triggers an upward movement under the effect of topography, resulting in a rapid enhancement of the ALI. Low-level water vapor convergence and upward moisture work together to form a pattern of low-level convergence and middle-level divergence. The increase in LLJI and VWS 30–60 minutes prior to the onset is conductive to heavy rainfall, showing that the development of low-level perturbations an obvious lower-level dominant mechanism.
- (2) The WSHR in the central region typically occurs on the complex urban subsurface, with complex wind fields and earlier appearance of the precursor signals. Wind profiles show that there are double LLJs at 700 hPa and 900 hPa, where moisture transport and VWS are concentrated. a large low-level VWS due to the high roughness, rapidly weakening wind speeds below 1 km, and the presence of significant rapids between 2 and 4 km. The BLH is significantly enhanced in the urban center (LG), and starts to perturb and rise before the rainfall, and then falls. Evolutionary feature of initial ascent followed by descent reflects the accumulation and triggering process of energy within the boundary layer. Enhanced turbulent mixing strengthens local updrafts and leads to boundary layer lifting 3 hours prior to rainfall. Scattered convection may have already developed in the vicinity or upstream 1.5 hours before rainfall. Precipitation generated by this convection leads to evaporative cooling, forming cold pools, which were important in triggering and maintaining the MCSs (Wang et al., 2014). The outflow from these cold pools affects the local area, causing a rapid decrease in the BLH while lifting warm, moist air. The vertical transport term at 500–750 hPa shows upward motion, which is associated with coupling between the lower and upper jet streams. This manifests as a mechanism of low-level convergence and high-level divergence that facilitates rainfall formation.
- (3) The eastern region is controlled by the South China Sea and the periphery of the subtropical high, exhibiting distinct characteristics of upper-level moisture transport. Wind profile analysis shows relatively weak low-level winds in this region, while a southwestward jet stream is active between 500–700 hPa. The moisture flux vector at this altitude shows an inclined upward pattern. Before precipitation, wind direction above 1 km is consistent with height, and vertical disturbances are relatively weak. Vertical moisture integration and flux analysis reveal that a wide range and strong intensity of moisture transport exists over this region. The upper-level jet stream dominates the rapid movement and accumulation of moisture, leading to a strong convergence zone in the lower levels and widespread divergence in the middle to upper levels, reflecting the mechanism of high-level control and low-level response. In addition, the LLJI is generally large and has a long duration in the eastern region, indicating that the persistent and stable jet stream contributes to steady moisture supply.



495

500

505

510

515

520



In conclusion, the genesis of WSHR in Guangdong manifests considerable regional disparity, predominantly attributable to variations in triggering mechanisms, altitudes of water vapor transport, and boundary layer properties. In the western sector, water vapor predominantly accumulates in the lower stratum, primarily elevated through orographic influences and convergence processes. The central region is characterized by a dual LLJ configuration. Rainfall is triggered by local thermal disturbances integrated with wind field coupling. The boundary layer height is most significantly affected by cities and changes of the BLH. Water vapor in the eastern region is mainly transported in the middle and upper layers, influenced by the upper-level jet and disturbances at the edge of the subtropical high.

5.2 Potential application of precursor signals in nowcasting

Quantitative precursor signals are extracted from wind profile radar data in high spatiotemporal resolutions, which provide a reference for advance nowcasting of the WSHR. It is found that most of the key meteorological factors begin to change significantly within 0.5–2 hours before the rainstorms, with obvious 'inflection point' characteristics: ALI uplift often occurs 60–90 minutes before precipitation; LLJI rapid intensification occurs 60–90 minutes before precipitation; BLH increase occurs about 80–100 minutes in advance; and increase in the BLH occurs about 80–100 minutes in advance. The rapid intensification of the LLJI occurs within 60–90 minutes; the BLH uplift process occurs about 80–100 minutes in advance, and the rapid change in VWS after a sustained increase indicates the release of vertical instability. These near-term changes are conductive for the short-term and nowcasting warning model of rainstorms.

6 Concluding Remarks

In this study, the precursor signals of the 2019 WSHR in Guangdong are systematically analyzed based on wind profile radar and high-density ground-based observational data. Results reveal the atmospheric dynamic processes before the occurrence of WSHR, and point out that there are significant seasonal and regional differences in the precursor signals of WSHR, which are mainly influenced by meteorological factors such as low-level jets, boundary layer height, atmospheric lifting intensity and vertical wind shear, and the signal characteristics in different regions are closely related to monsoon activities, geographical factors, etc. The main conclusions are shown as follows.

(1) Through analyzing the precursor signals of the wind field, vertical structure and boundary layer height in different regions, it can be seen that the warning signals of heavy rainfall in the warm sector usually appear 1–2 hours before the onset of rainfall and show different structural characteristics. Precipitation in the western region is influenced by low-level warm humid airflow and topographic uplift, and the signals are prominent in the lower layers. Rainfall in central region is influenced by urban effects and double low-level jets, and the signals are complex and occur earlier. Precipitation in the eastern region is influenced by high-altitude jets and water vapor transport, and the signals tend to be dominated by the upper layers.



535

540

545



- 525 (2) The main factors affecting regional differences in precursor signals are monsoon and geography. There is variability in the response to precursor signals in different regions. Precipitation in the western region relies more on low-level water vapor accumulation and topography; rainfall in the central region relies more on the urban heat island effect and boundary layer changes; and the precursor signals in the eastern region are more related to changes in high-altitude rapids and the oblique transport properties of water vapor. In addition, the activity of the summer monsoon in the South China Sea affects formation conditions of the WSHR, especially in enhancing water vapor transport and the development of low-level jets, which plays an important role in regulating the temporal and spatial distribution of the precursor signals.
 - (3) It is shown that the thermal and dynamical effects of urban agglomerations significantly change the boundary layer structure, which in turn affects the performance of the precursor signals. The urban heat island effect can advance the onset of boundary layer instability and enhance local instability and convective activity, making the precursor signals in the central region more localized and placing higher demands on nowcasting.
 - (4) Precursor signals have application potential in nowcasting. A refined forecast of heavy precipitation in different regions can be achieved by optimizing weights of regional precursor signals. In particular, the ability to forecast extreme precipitation can be significantly improved through developing a multi-factor composite forecasting system integrated with an intelligent early warning platform.

There are still some shortcomings in this study, the extraction thresholds and discrimination methods of precursor signals need to be standardized, the precursor signal characteristics of different types of WSHR have not been fully covered, and the study of urban dynamical mechanisms is still insufficient. In the future, the study will strengthen the exploration of the coupling mechanism of different scale dynamical processes, and further combine with machine learning and other methods, so that it can be more effectively used in storm forecasting operations.



550



Data availability

The land cover data are available at https://zenodo.org/record/5816591 (Yang & Huang, 2021). The ERA5 data can be downloaded from https://cds.climate.copernicus.eu/datasets/reanalysis-era5-pressure-levels?tab=overview (Hersbach et al., 2023).

Author contributions.s

The study was completed with close cooperation between all authors. YY conceived of the idea for this work. ZH designed the methodology. WL performed the main analysis. WL and ZH drafted the original manuscript with contributions from SL, XB, YY, LS, SX, CL, YY and provided useful suggestions and comments for the study and helped revise the manuscript.

555 Financial support

This work has been supported by the National Natural Science Foundation of China (grant nos. 42222503, and 42175098), and Guangdong Provincial Marine Meteorology Science Data Center (grant no. 2024B1212070014).

Competing interests

The authors declare that there is no conflict of interest.

560 References

Angevine, W. M., White, A. B., and Avery, S. K.: Boundary-layer depth and entrainment zone characterization with a boundary-layer profiler, Boundary-Layer Meteorol, 68, 375–385, https://doi.org/10.1007/BF00706797, 1994.

Bellamy, J. C.: Objective Calculations of Divergence, Vertical Velocity and Vorticity, https://doi.org/10.1175/1520-0477-30.2.45, 1949.

Burk, S. D.: Refractive Index Structure Parameters: Time-Dependent Calculations Using a Numerical Boundary-Layer Model, 1980.

Chen, T. and Zhang, D.-L.: A 7-Year Climatology of Warm-Sector Heavy Rainfall over South China during the Pre-Summer Months, Atmosphere, 12, 914, https://doi.org/10.3390/atmos12070914, 2021.

Chen, Y., Chen, T., Wang, L., et al.: A review of the warm-sector rainstorms in China, Torrential Rain and Disasters, 38(5), 483–493, 2019.(in Chinese)

Ding, Y. H.: Monsoons Over China. Dordrecht, Kluwer Academic, 419 pp, 1994.





- Du, Y. and Chen, G.: Heavy Rainfall Associated with Double Low-Level Jets over Southern China. Part I: Ensemble-Based Analysis, https://doi.org/10.1175/MWR-D-18-0101.1, 2018.
- Du, Y., Zhang, Q., Ying, Y., and Yang, Y.: Characteristics of Low-level Jets in Shanghai during the 2008-2009 Warm Seasons as Inferred from Wind Profiler Radar Data, Journal of the Meteorological Society of Japan, 90, 891–903, https://doi.org/10.2151/jmsj.2012-603, 2012.
 - Du, Y., Chen, G., Han, B., Mai, C., Bai, L., and Li, M.: Convection Initiation and Growth at the Coast of South China. Part I: Effect of the Marine Boundary Layer Jet, Monthly Weather Review, 148, 3847–3869, https://doi.org/10.1175/MWR-D-20-0089.1, 2020a.
- Du, Y., Chen, G., Han, B., Bai, L., and Li, M.: Convection Initiation and Growth at the Coast of South China. Part II: Effects of the Terrain, Coastline, and Cold Pools, https://doi.org/10.1175/MWR-D-20-0090.1, 2020b.
 - Gao, Z., Zhu, J., Guo, Y., Luo, N., Fu, Y., and Wang, T.: Impact of Land Surface Processes on a Record-Breaking Rainfall Event on May 06–07, 2017, in Guangzhou, China, Journal of Geophysical Research: Atmospheres, 126, e2020JD032997, https://doi.org/10.1029/2020JD032997, 2021.
- Heo, B.-H., Jacoby-Koaly, S., Kim, K.-E., Campistron, B., Benech, B., and Jung, E.-S.: Use of the Doppler Spectral Width to Improve the Estimation of the Convective Boundary Layer Height from UHF Wind Profiler Observations, 2003.
 - Higgins, R. W., Yao, Y., Yarosh, E. S., Janowiak, J. E., and Mo, K. C.: Influence of the Great Plains Low-Level Jet on Summertime Precipitation and Moisture Transport over the Central United States, 1997.
- Huang, S. S.: Heavy Rainfall over Southern China in the Pre-Summer Rainy Season, Guangdong Science and Technology Press, 244 pp., 1986. (in Chinese)
 - Huang, Y., Liu, Y., Liu, Y., Li, H., and Knievel, J. C.: Mechanisms for a Record Breaking Rainfall in the Coastal Metropolitan City of Guangzhou, China: Observation Analysis and Nested Very Large Eddy Simulation With the WRF Model, JGR Atmospheres, 124, 1370–1391, https://doi.org/10.1029/2018JD029668, 2019.
- Kotthaus, S., Bravo-Aranda, J. A., Collaud Coen, M., Guerrero-Rascado, J. L., Costa, M. J., Cimini, D., O'Connor, E. J., Hervo, M., Alados-Arboledas, L., Jiménez-Portaz, M., Mona, L., Ruffieux, D., Illingworth, A., and Haeffelin, M.: Atmospheric boundary layer height from ground-based remote sensing: a review of capabilities and limitations, Atmos. Meas. Tech., 16, 433–479, https://doi.org/10.5194/amt-16-433-2023, 2023.
- Li, C., Zhang, X., Guo, J., Yu, Q., and Zhang, Y.: Decadal variation and trend of boundary layer height and possible contributing factors in China, Agricultural and Forest Meteorology, 347, 109910, https://doi.org/10.1016/j.agrformet.2024.109910, 2024a.
 - Li, N., Guo, J., Wu, M., Zhang, F., Guo, X., Sun, Y., Zhang, Z., Liang, H., and Chen, T.: Low-Level Jet and Its Effect on the Onset of Summertime Nocturnal Rainfall in Beijing, Geophysical Research Letters, 51, e2024GL110840, https://doi.org/10.1029/2024GL110840, 2024b.
- Liang, Z. and Gao, S.: Organized Warm-Sector Rainfall in the Coastal Region of South China in an Anticyclone Synoptic Situation: Observational Analysis, J Meteorol Res, 35, 460–477, https://doi.org/10.1007/s13351-021-0157-4, 2021.
 - Liu, B., Guo, J., Gong, W., Shi, L., Zhang, Y., and Ma, Y.: Characteristics and performance of wind profiles as observed by the radar wind profiler network of China, Atmospheric Measurement Techniques, 13, 4589–4600, https://doi.org/10.5194/amt-13-4589-2020, 2020.





- Liu, R., Sun, J., and Chen, B.: Selection and Classification of Warm-Sector Heavy Rainfall Events over South China, Chinese Journal of Atmospheric Sciences, 43(1), 119–130, doi:10.3878/j.issn.1006-9895.1803.17245, 2019.(in Chinese)
 - Liu, S. Y., Zheng, Y. G., and Tao, Z. Y.: The analysis of the relationship between pulse of LLJ and heavy rain using wind profiler data, J. Trop. Meteor., 19(3), 285–290, doi:10.3969/j.issn.1004-4965.2003.03.008, 2003.(in Chinese)
- Lolli, S., Delaval, A., Loth, C., Garnier, A., and Flamant, P. H.: 0.355-micrometer direct detection wind lidar under testing during a field campaign in consideration of ESA's ADM-Aeolus mission, Atmospheric Measurement Techniques, 6, 3349–3358, https://doi.org/10.5194/amt-6-3349-2013, 2013.
 - Luo, Y., Zhang, R., Wan, Q., Wang, B., Wong, W. K., Hu, Z., Jou, B. J.-D., Lin, Y., Johnson, R. H., Chang, C.-P., Zhu, Y., Zhang, X., Wang, H., Xia, R., Ma, J., Zhang, D.-L., Gao, M., Zhang, Y., Liu, X., Chen, Y., Huang, H., Bao, X., Ruan, Z., Cui, Z., Meng, Z., Sun, J., Wu, M., Wang, H., Peng, X., Qian, W., Zhao, K., and Xiao, Y.: The Southern China Monsoon Rainfall Experiment (SCMREX), https://doi.org/10.1175/BAMS-D-15-00235.1, 2017.
- Ning, G., Luo, M., Bi, X., Liu, Z., Zhang, H., Huang, M., Huang, X., Yang, Y., and Wu, S.: Large-scale moisture transport and local-scale convection patterns associated with warm-sector heavy rainfall over South China, Atmospheric Research, 285, 106637, https://doi.org/10.1016/j.atmosres.2023.106637, 2023.
 - Pu, Y., Hu, S., Luo, Y., Liu, X., Hu, L., Ye, L., Li, H., Xia, F., and Gao, L.: Multiscale Perspectives on an Extreme Warm-Sector Rainfall Event over Coastal South China, Remote Sensing, 14, 3110, https://doi.org/10.3390/rs14133110, 2022.
- Seibert, P., Beyrich, F., Gryning, S.-E., Joffre, S., Rasmussen, A., and Tercier, P.: Review and intercomparison of operational methods for the determination of the mixing height, Atmospheric Environment, 34, 1001–1027, https://doi.org/10.1016/S1352-2310(99)00349-0, 2000.
 - Stensrud, D. J.: Importance of Low-Level Jets to Climate: A Review, 1996.
- Sun, J., Zhang, Y., Liu, R., Fu, S., and Tian, F.: A Review of Research on Warm-Sector Heavy Rainfall in China, Adv. Atmos. Sci., 36, 1299–1307, https://doi.org/10.1007/s00376-019-9021-1, 2019.
 - Trier, S. B., Davis, C. A., Ahijevych, D. A., Weisman, M. L., and Bryan, G. H.: Mechanisms Supporting Long-Lived Episodes of Propagating Nocturnal Convection within a 7-Day WRF Model Simulation, https://doi.org/10.1175/JAS3768.1, 2006.
- Wang, C., Chen, X., and Zhao, K.: Extreme local mesoscale convective systems over the South China coast during the warm season, Quart J Royal Meteoro Soc, e4959, https://doi.org/10.1002/qj.4959, 2025.
 - Wang, H., Luo, Y., and Jou, B. J.-D.: Initiation, maintenance, and properties of convection in an extreme rainfall event during SCMREX: Observational analysis, Journal of Geophysical Research: Atmospheres, 119, 13,206-13,232, https://doi.org/10.1002/2014JD022339, 2014.
- Wu, Y., Guo, J., Chen, T., and Chen, A.: Forecasting Precipitation from Radar Wind Profiler Mesonet and Reanalysis Using the Random Forest Algorithm, Remote Sensing, 15, 1635, https://doi.org/10.3390/rs15061635, 2023.
 - Xian, T., Guo, J., Zhao, R., Guo, X., Li, N., Sun, Y., Zhang, Z., Su, T., and Li, Z.: Impact of Urbanization on Mesoscale Convective Systems: Insights From a Radar Wind Profiler Mesonet, Theoretical Analyses, and Model Simulations, Journal of Geophysical Research: Atmospheres, 129, e2024JD042294, https://doi.org/10.1029/2024JD042294, 2024.





- Zeng, W., Chen, G., Du, Y., and Wen, Z.: Diurnal Variations of Low-Level Winds and Precipitation Response to Large-Scale Circulations during a Heavy Rainfall Event, https://doi.org/10.1175/MWR-D-19-0131.1, 2019.
 - Zhang, L., Ma, X., Zhu, S., Guo, Z., Zhi, X., and Chen, C.: Analyses and applications of the precursor signals of a kind of warm sector heavy rainfall over the coast of Guangdong, China, Atmospheric Research, 280, 106425, https://doi.org/10.1016/j.atmosres.2022.106425, 2022a.
- Zhang, M. and Meng, Z.: Warm-Sector Heavy Rainfall in Southern China and Its WRF Simulation Evaluation: A Low-Level-Jet Perspective, https://doi.org/10.1175/MWR-D-19-0110.1, 2019.
 - Zhang, M., Rasmussen, K. L., Meng, Z., and Huang, Y.: Impacts of Coastal Terrain on Warm-Sector Heavy-Rain-Producing MCSs in Southern China, Monthly Weather Review, 150, 603–624, https://doi.org/10.1175/MWR-D-21-0190.1, 2022b.
 - Zhong, S. and Chen, Z.: The Impacts of Atmospheric Moisture Transportation on Warm Sector Torrential Rains over South China, Atmosphere, 8, 116, https://doi.org/10.3390/atmos8070116, 2017.
- Zhou, X., Cheng, Z., Li, H., and Hu, D.: Comparison between the Roles of Low-Level Jets in Two Heavy Rainfall Events over South China, J Meteorol Res, 36, 326–341, https://doi.org/10.1007/s13351-022-1159-6, 2022.